Mineralium Deposita (2024) 59:815–835
https://doi.org/10.1007/s00126-023-01232-5

ARTICLE

The shallow marine VMS copper deposit of Yushui, Eastern Guangdong, South China: evidence from geology, geochronology, and geochemistry

Gang Chen[1] · Xiuqing Yang[2] · Changhui Ke[1] · Yanwen Tang[3] · Maohong Chen[1]

Received: 29 December 2022 / Accepted: 27 October 2023 / Published online: 6 December 2023
© The Author(s), under exclusive licence to Springer-Verlag GmbH Germany, part of Springer Nature 2023

Abstract

Many massive sulfide deposits have been discovered in the Upper Paleozoic rift-related volcaniclastic sequence in South China, among which the Yushui copper deposit is the most important due to its high grade. The deposit has been variably attributed as SEDEX (sedimentary exhalative) or MVT (Mississippi valley type). The Yushui copper deposit in Guangdong (South China) contains stratiform bornite-chalcopyrite orebodies (102.1 kt Cu @ 3.5%, 186.6 kt Pb @ 4.29%, 117.6 kt Zn @ 2.91%, and 339 t Ag @ 112 g/t) developed along the contact between Upper Carboniferous dolostone and Lower Carboniferous pebbly quartz sandstone, which indicates a shallow marine deposition environment. The Yushui deposit comprises an upper massive sulfide orebody and a lower stockwork orebody with intense alteration. In this study, we newly identified Carboniferous tuffs and syn-volcanic faults in the footwall, and exhalites in the hanging-wall. Hematite from the Cu ores yielded a U-Pb age of 320 ± 15 Ma (MSWD = 2.1, n = 57), and hydrothermal dolomite yielded a Sm-Nd isochron age of 308.1 ± 4.6 Ma (n = 7; MSWD = 0.94), which constrains the timing of mineralization at Yushui. These ages are coeval with the Carboniferous host rocks. Combining the evidence from the geological features (syn-volcanic faults, volcanic rocks, exhalites) and hematite trace element compositions, we suggest that the Yushui is a shallow marine VMS (volcanogenic massive sulfide) deposit. The Sr-Nd isotope composition of hydrothermal dolomite (ε_{Nd} ~−12) indicates that the ore-forming materials were originated from the crustal basement. The Yushui copper deposit was likely formed during the Late Carboniferous continental back-arc extension in eastern South China. The regional extension may have caused enhanced heat flow, which promoted fluid convection in the basement rocks. In addition, we suggest that volcanic rocks and disseminated chalcopyrite-pyrite mineralization in the Lower Carboniferous quartz sandstone and exhalites are good indicators for regional VMS prospecting.

Keywords Hematite U-Pb dating · Dolomite Sm-Nd dating · Shallow marine VMS deposit · Carboniferous · Yushui copper deposit

Introduction

It has long been suggested that volcanogenic massive sulfide (VMS) deposits or modern seafloor massive sulfide deposits (SMS) are mainly formed in deep water environments (e.g., Franklin et al. 2005; Hannington et al. 2005, 2011; Cherkashov 2011; Schulz 2010; Shanks 2012; German et al. 2016; Petersen et al. 2016). In contrast, it is commonly considered that the fluids vented in shallow marine environments would boil readily, and are thus non-conducive to sulfide deposition and VMS/SMS formation (Cathles 2010; Monecke et al. 2014). However, the various ocean drilling programs (Deep Sea Drilling Program, DSDP; Ocean Drilling Program, ODP; Integrated Ocean Drilling Program, IODP) have

Editorial handling: S.-Y. Jiang

✉ Maohong Chen
mhchen666@163.com

[1] MNR Key Laboratory of Metallogeny and Mineral Assessment, Institute of Mineral Resources, Chinese Academy of Geological Sciences, Beijing 100037, China

[2] School of Earth Science and Resources, Chang'an University, Xi'an 710054, China

[3] State Key Laboratory of Ore Deposit Geochemistry, Institute of Geochemistry, Chinese Academy of Sciences, Guiyang 550081, China

observed hydrothermal activities in shallow marine settings (< 1000 m depth), with sulfide accumulation in the early-stage mid-ocean ridge opening (e.g., East African Rift, Red Sea-Atlantis II Deep, Lake Baikal) (Bonatti et al. 1972; Crane et al. 1991; Tiercelin et al. 1993) or in the landward part of the ridge (e.g., northern Iceland, Salton Sea) (Mckibben and Elders 1985; Fricke et al. 1989; Olafsson et al. 1989; Botz et al. 1999; Canet et al. 2005; Camprubí et al. 2007). Therefore, such shallow marine settings associated with early-stage basin expansion have the potential to produce metal sulfide deposits (Halley and Roberts 1997; Marani et al. 1997, 2002; Savelli et al. 1999; Dekov and Savelli 2004; Baker 2004; de Ronde et al. 2014). In shallow marine environments, vein-type and stockwork (but usually not stratiform massive) orebodies can be formed, which is different from typical VMS systems (Hannington et al. 1997; Hou et al. 2003; Lusty et al. 2017). Although fluid boiling could cause metal loss, it could also contribute to metal precipitation at/near the seafloor in shallow-water hydrothermal systems (Hannington 2021; Falkenberg et al. 2021; Schaarschmidt et al. 2021). However, extensive lateral replacement could be widespread in highly permeable subseafloor rocks, contributing to massive ore formation (Hannington et al. 1999a, b, c; Tornos 2006).

The Yushui copper deposit in eastern Guangdong province, South China, is a high-grade copper-polymetallic deposit, with 3- to 7-m-thick massive bornite and chalcopyrite orebodies (Cu grade, 10–53%). Yushui contains a reserve of 102.1 kt Cu @ 3.5%, 186.6 kt Pb @ 4.29%, 117.6 kt Zn @ 2.91%, and 339 t Ag @ 112 g/t (He 1990). The ore genesis has been variably interpreted as of syngenetic exhalative-sedimentary type (sediment-hosted massive sulfide deposit or SEDEX) (Gu and Xu 1986; He 1990; Gu et al. 2007; Huang et al. 2015a, b) or of epigenetic hydrothermal type (MVT or late hydrothermal replacement) (Chen et al. 1994; Cai et al. 1996; Liu 1997; Cheng et al. 2014). Recently, we have identified geological evidence, such as volcanic rocks, fluid channels, syn-volcanic faults, and exhalites at Yushui, and proposed that the deposit may be classified as VMS-type (Chen et al. 2021). In this study, we present new hematite U–Pb and dolomite Sm–Nd dates to constrain the ore-formation age at Yushui. We also integrate geological, geochronological, and geochemical evidence to further discuss the genesis of the Yushui deposit as an example for shallow marine massive sulfide mineralization.

Regional geology

The Yushui copper deposit is located in the middle section of the late Paleozoic Yong'an–Meizhou–Huizhou rift basin (Guangdong BGMR 1988; Ren 1990). The basin extends NNE-SSW for about 500 km (~150 km wide), and is bounded by the Zhenghe–Dapu and Shaowu–Heyuan faults to the east and west, respectively (Huang et al. 2015a, b) (Fig. 1).

The regional tectono-stratigraphy comprises three phases: (1) The Caledonian (Sinian and Cambrian) folded basement is composed of continental shelf-slope facies flysch clastic rocks, which were strongly folded and low-grade metamorphosed; (2) Hercynian–Indosinian (Devonian and Carboniferous) coastal and shallow marine clastic, carbonate, and coal-bearing rocks with local volcanic interbeds. Over ten Fe-Mn deposits and Cu-Pb-Zn polymetallic deposits are distributed along the contact between the Lower Carboniferous sandstone and the overlying Upper Carboniferous carbonate rocks (Xun et al. 1996; Gu et al. 2007); (3) Yanshanian (Jurassic–Cretaceous) thick continental volcanic rocks and terrestrial red beds.

From the Devonian to Triassic, South China may have continued to extend, forming a series of fault depressions with thick terrigenous clastic and carbonate deposits and minor volcanic interbeds, indicating the starting of continental margin rift basin sedimentation (Wang 2005; Wang and Jin 2000). The Indosinian (Triassic) movement in South China had ended marine sedimentation, while the Jurassic period saw the beginning of Paleo-Pacific subduction beneath Eastern China, forming a series of volcanic rift basins (Liu et al. 2018; Jia et al. 2018).

Deposit geology

Stratigraphy

The Yushui deposit, which was discovered in 1985, is a concealed copper-lead-zinc polymetallic deposit (116° 10′ 50″E, 24° 25′ 15″N). The major exposed stratigraphy comprises the Upper Jurassic Gaojiping Group (J_3gj) and Lower Cretaceous Guancaohu Group (K_1gn^a). The former consists of basalt, andesite, rhyolite, and tuff with tuffaceous sandstone and argillaceous siltstone interlayers; the latter contains volcanic rocks, arkose, and silty shale with dacitic tuff interlayers. In addition, Middle and Upper Devonian ($D_{2\text{-}3}$, ~100 m thick) and Carboniferous sequences are also exposed locally. The Middle and Upper Devonian sequence comprises gray-white quartz sandstone that unconformably overlies the Cambrian basement.

Stratabound orebodies are located between the Zhongxin Formation (C_1z) purplish-red quartz sandstone and the Hutian Formation (C_2ht) dolostone (Figs. 2 and 3). The Zhongxin Formation becomes grayish white with decreasing hematite content away from the orebodies. The sandstone of the Zhongxin Formation is overlain by littoral pebbly quartz sandstone (thickness, 5–30 cm) (ESM 1a), which contains 20–40 vol% pebbles and randomly oriented quartz (ESM 1b).

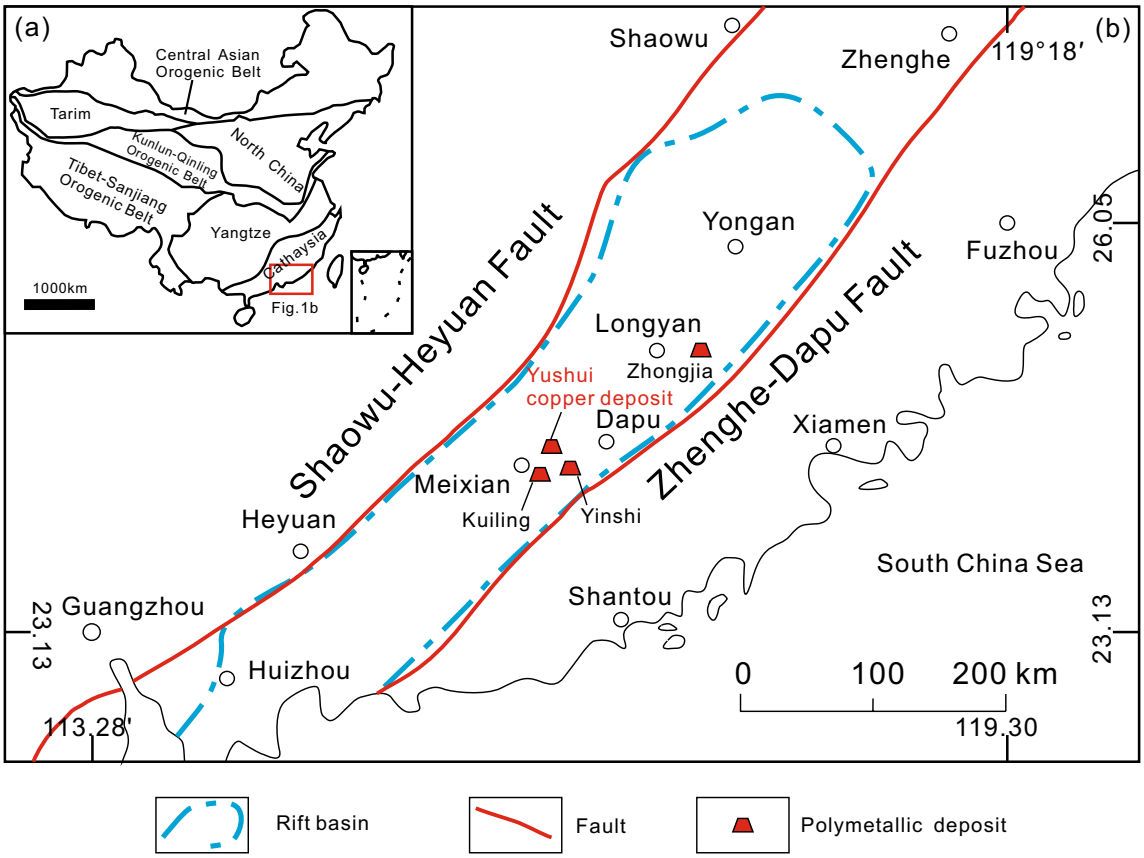

Fig. 1 (**a**) Simplified geological map showing the location of the study area. (**b**) Regional geological map of the Yong'an-Meizhou-Huizhou depression (modified after He 1990; Huang et al. 2015a, b; and Chen et al. 2021)

The Hutian Formation (C_2ht) is about 300 m thick and dominated by gray dolostone and calcareous dolostone, with light-gray limestone and bioclastic limestone interbeds. Large fossils, such as *corals* and *Chaetetida*, have been reported in this formation, suggesting a shallow marine depositional environment (ESM 1e, f). The orebody footwall and hanging-wall was likely deposited in a littoral and shallow-water environment, respectively. This likely reflects a sudden seawater deepening, possibly via basin extension.

Structures

Both the Devonian and Carboniferous strata show NE-dipping monoclinic structures. Local structures include mainly two sets of NNE- and EW-striking normal faults. Local normal/transtensional faults strike NNE to EW, which control the shape of the Yanshanian volcanic basin (Figs. 2 and 3). Fieldwork indicates that many orebodies are cut and displaced by a series of near EW- and NE-trending faults.

Igneous rocks

Intrusions

Local magmatic rocks include mainly Yanshanian (Jurassic) dikes (outcrop size, 20–300 cm wide, up to 10 m long), with compositions including granite porphyry, quartz porphyry, and diabase. The magmatic rocks clearly cut the orebodies, indicating that they are post-ore. Li et al. (2019) reported LA-ICP-MS zircon U-Pb ages of 128.4 ± 1.0 Ma for the granite-porphyry and 59.3 ± 2.5 Ma for the diabase.

Volcanic rock

The presence of volcanic rocks and their compositions are key criteria for classifying VMS deposits. For example, Cyprus-type and Kuroko-type deposits are mainly related to mid-ocean ridge basalts (MORB) and island-arc bimodal suites, respectively (Hou et al. 2003; Franklin et al. 2005). At Yushui, our field work has found at least two volcanic layers in the quartz sandstone footwall, along with volcanic

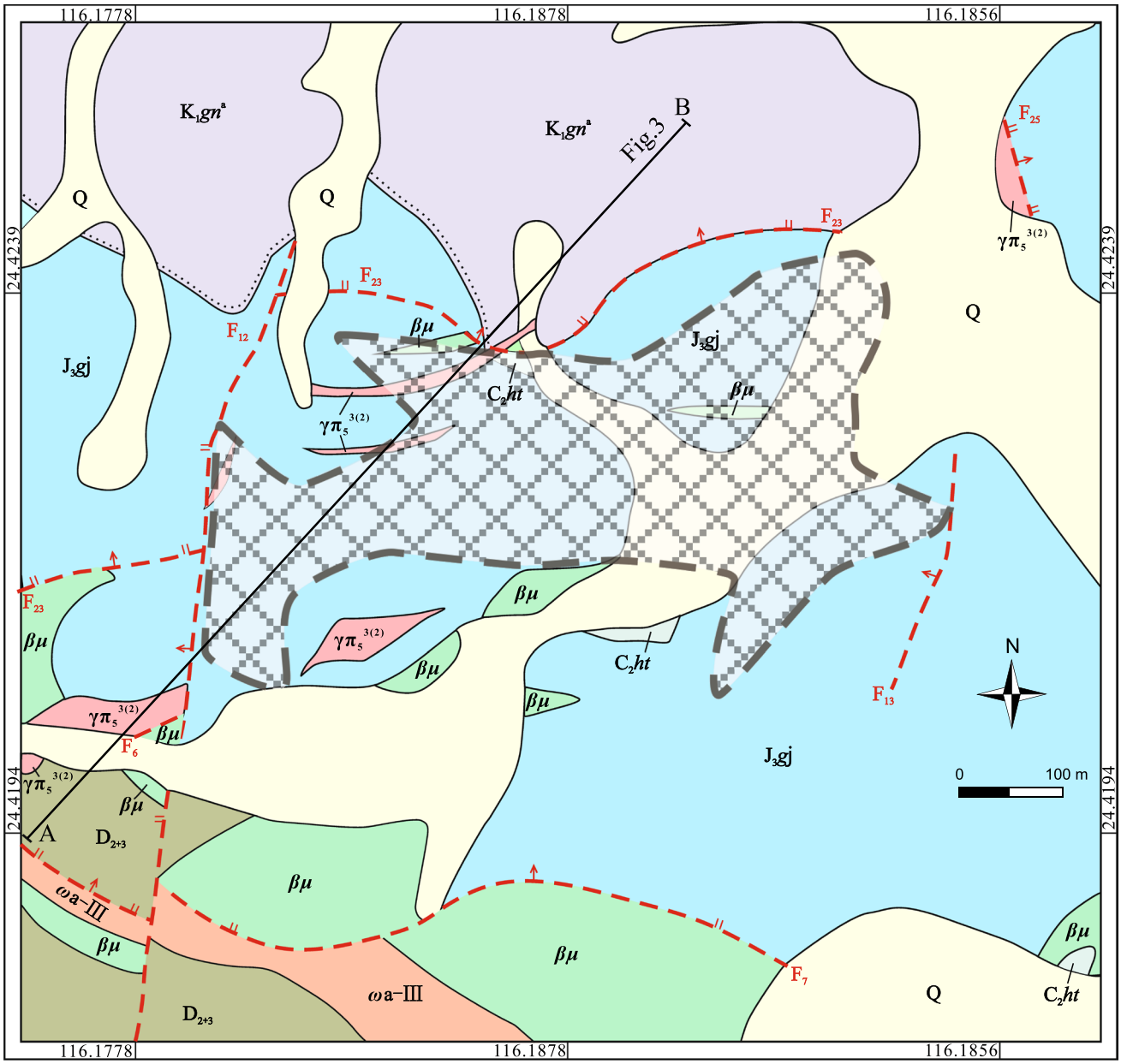

Fig. 2 Geological map of the Yushui deposit (modified after No. 723 Geological Team of the Bereau of Geology and Mineral Resources of Guangdong Province 1988 and Chen et al. 2021)

ash mounds and volcanic channels (Figs. 4 and 5a) (Chen et al. 2021).

A volcanic ash bed is 0–20 cm thick which is grayish-white in color. Two layers of volcanic rocks developed parallel to the stratiform orebody. The layer is 15–20 cm thick near the vent, and gradually thins out outward, forming a low gentle mound (Fig. 5a). A chalcopyrite lens is sandwiched in the tuff near the vent, about 5 × 10 cm in size. The volcanic channel is flared and filled with unconsolidated volcanic ash (Fig. 5b). The volcanic rocks (basaltic) have vitroclastic

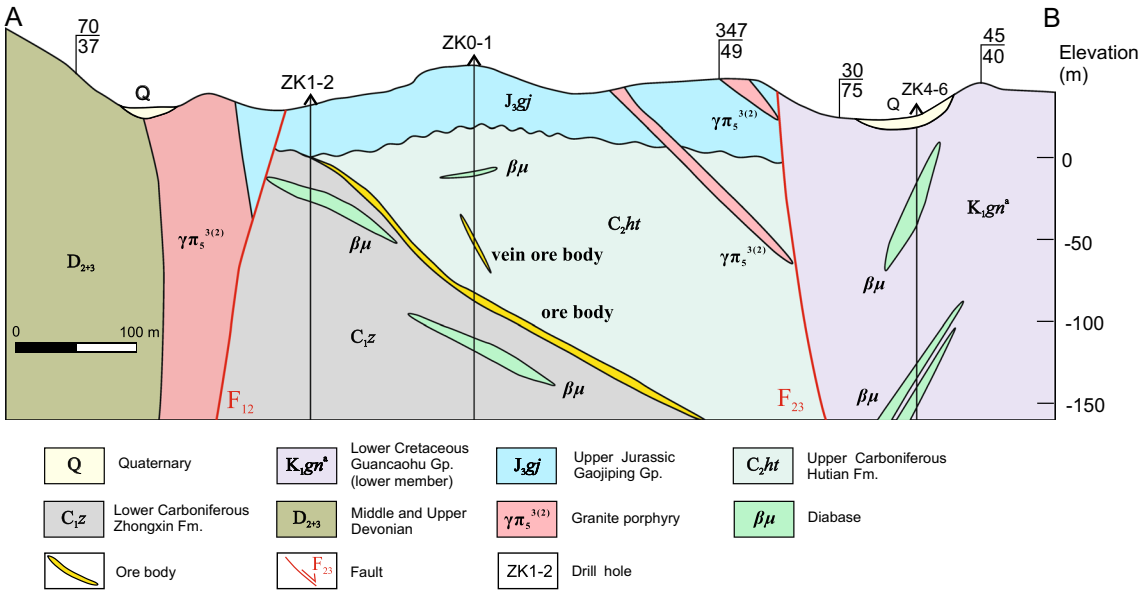

Fig. 3 Geological profile of exploration line A–B (modified from No. 723 Team of Guangdong BGMR 1988; He 1990; and Chen et al. 2021). See Figure 2 for the profile location

texture, with the main metallic and non-metallic minerals being chalcopyrite and sericite, respectively (Fig. 7a). The volcanic rocks are quartz crystal fragment tuff (Fig. 7b).

The analysis of the major elements of six tuff samples shows that one sample has anomalous SiO_2 content of 76 wt%, which may be due to mixing with quartz sandstone (Chen et al. 2021). After normalization, the SiO_2 content of the other five samples ranges from 44.2 to 62.0 wt% (ESM 2A), which roughly belongs to the category of basalt to andesite.

Exhalites

The exhalites at Yushui are featured by a red chert-jasperite suite in the upper part of the massive orebody (Fig. 4). Where the orebody gradually pinches out along strike, the sulfide (pyrite-chalcopyrite-bornite-sphalerite-galena) ores are lensoidal shaped and distributed in the red exhalites (Fig. 5c). The exhalites contain locally red jasper, which is in direct contact with the underlying orebody. In hand-specimen or outcrop scale, jasperite and massive ore show a distinct stratiform vertical change: (lower part) pyrite-chalcopyrite layer, (middle part) galena-sphalerite ore, and (upper part) red jasperite. The contact between jasperite and the underlying lead-zinc ore displays flame structure, suggesting a sedimentary origin and zone refining (Fig. 5d), as supported by the oolitic hematite in the red jasper (Fig. 7c).

Exhalites at Yushui are similar to the mafic-siliciclastic formations of some VMS deposits, but are characterized by the widespread presence of hematite and siderite. The stratiform ore contains volcanic rocks and exhalites, with clear contacts between them (Fig. 5e). Both jasperite and chert contain a large amount of fine-grained/dusty hematite, giving the rock its characteristic red color.

Microscopically, both siderite and hematite are euhedral, and they are closely intergrown with each other (Fig. 7d). Most hematite grains are coarse with needle or radial shape, and some are fine-grained or dusty. Jasperite is mostly composed of 99 % quartz (Fig. 7e), but siderite and dolomite may reach 50 % (Fig. 7f). Jasperite is rich in SiO_2 (>90.6 wt%) and Fe ($FeO+Fe_2O_3$>3.95 wt%). The trace-element composition corresponds to precipitates from hot springs (He 1990).

Syn-volcanic faults

Syngenetic faults in VMS deposits are important in controlling the distribution of sedimentation and volcanism in regional basins, and in providing channels for deep ore-forming fluids, thus playing a key role in both diagenesis and mineralization (Herzig and Hannington 1995; Hou et al. 2003; Franklin et al. 2005).

At Yushui, syn-volcanic faulting is observed in several outcrops, which show large thickness variation of the orebodies and volcanic-sedimentary rocks on both sides of the faults (Fig. 5f). In addition, the Cu orebody is crosscut by syn-volcanic faults, forming drag folds (Fig. 5g). The syn-volcanic faults strike SW and dip NE, (sub-)parallel to the main fluid channel (Fig. 6a). Syngenetic faults do not cut the overlying copper orebody or dolostone, and control the fluid/volcanic conduits, consistent with a syn-volcanic origin.

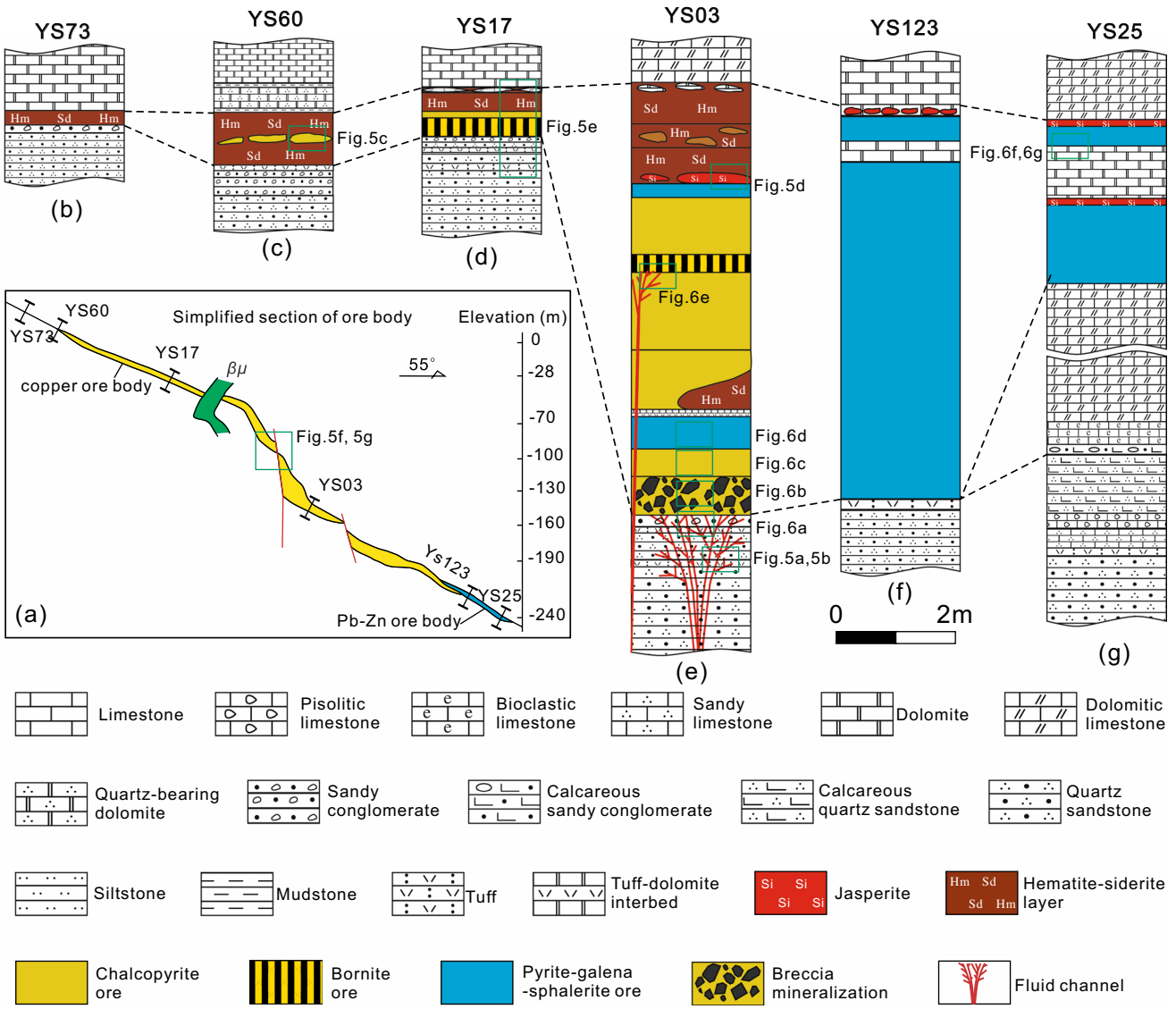

Fig. 4 Stratigraphic comparison of the ore host for the Yushui stratiform orebodies (modified from Chen et al. 2021). Red exhalites overlie conformably the orebody. Volcanic rocks gradually pinch out toward the margin. Fluid channel facies and quartz veinlets only appear in the thicker/larger middle section of the orebody. **a** Schematic stratigraphic sections, showing the location of YS73 **b**, YS60 **c**, YS17 **d**, YS03 **e**, YS123 **f**, and YS25 **g**. Locations of Figures 5 and 6 are also marked

Mineralization zones

The ore types include massive ores along the dolomite-quartz sandstone interface, stringer ores (in No. 1 orebody) in the quartz sandstone footwall, and minor vein ores that cut the stratigraphy (No. 2 and No. 3 orebody). No. 1 orebody is stratiform, striking NW-SE and dipping gently with 10 to 25°. The orebody is 150–250 m along strike and 500 m along dip, with an average thickness of 5.95m and average grade of 3.5% Cu, 4.29% Pb, 2.91% Zn, and 112 g/t Ag. No. 1 orebody accounts for 84.2% of the total ore reserve at Yushui. The No. 2 and No. 3 vein orebodies are smaller, and their disseminated ores occur in steep fractures and dikes, which cut No. 1 orebody and are late mineralization products (out of the scope of this study, for detailed descriptions see Chen et al. 2023). It is noteworthy that HREE (Y) and U mineralization is commonly developed in the Yushui No. 1, 2, and 3 orebodies (Liu et al. 2023a, 2023b), and that the HREE mineralization overprints on the stratiform ores (Chen et al. 2023).

Two main sulfide ore zones have been identified based on the host rocks, ore types, and mineral assemblages, i.e., a lower stringer zone in the Zhongxin Formation, and an upper massive zone with fluid channel-proximal copper ore and fluid channel-distal lead-zinc ore.

Stringer orebody and fluid channel

At least six nearly parallel fluid channels (with surrounding fan-shaped quartz stockwork) were identified in underground workings. These fluid channels are NS-/NNE-oriented (95–115°) and dipping steeply (dip angle, 84–86°). The main fluid channel narrows down from the upper part (width, 60–70 cm) to the lower part (width, 5–10 cm), extending vertically for over 10–20 m. The channel consists of sulfide (chalcopyrite, bornite, tetrahedrite) and hydrothermal quartz, with strong silicic, sericite, and chlorite alteration (Fig. 6a), clearly distinct from the purple quartz sandstone wallrocks. The sandstone at the top of the channel is also altered and bleached, creating an alteration cap of ~15 m wide. Quartz stockwork is developed and fanned out around the main body channel, forming a complete hydrothermal recharge system. The quartz stockwork does not cut the overlying massive copper ore lenses (Fig. 6a). The volcanic rocks near the fluid channels are the thickest and they contain the majority of copper ore lenses, suggesting that the fluid channels and volcanic channels may be contemporaneous.

The sandstone footwall is also silicified and sericitized with disseminated chalcopyrite. The stringer orebody and mineralized footwall are 1 to 10 m thick, with up to 5% copper. The ore grade and vein density drop steadily away from the vent center, suggesting a typical funnel-shape profile.

Massive sulfide lenses

The stratiform copper sulfide (incl. chalcopyrite and bornite) orebodies at Yushui are the thickest (up to 3–7 m) near the main fluid channel and thin out away from it, although the red exhalites are still present. The ores also transition gradually from Cu-dominated to Pb-Zn-dominated away from the vent center and with decreasing depths, showing metal zoning.

The copper lenses are the thickest (up to 3–7 m) above the main fluid channel, containing 2–3 rhythms (chalcopyrite → bornite → galena + sphalerite) (Fig. 4e), while the thin stratiform orebody in the west has a single rhythm (Fig. 4c). From floor to roof, chalcopyrite content gradually decreases, while galena and sphalerite contents gradually increase (Fig. 4e), and the single rhythm has similar variation characteristics. Chalcopyrite is mainly located on the floor of the copper lenses and is dominated by massive chalcopyrite (Fig. 6c) and cemented by hematite (Fig. 7g). Breccia-like ores (40–80 cm thick) are generally located at the base of massive chalcopyrite. There is a clear boundary between chalcopyrite and bornite and funnel-shaped interpenetration, similar to a fluid channel (Fig. 6e). Bornite includes a small amount of pyrite, chalcopyrite, galena, chalcocite, and renierite (Fig. 7h). Ore grade of individual bornite lenses can be as high as 53%, making them the richest ores at Yushui. The copper-lead-zinc ores (10–250 cm thick) are generally located in the upper part of the copper ore lenses, and with clear banded texture (Fig. 6d). Under reflected light microscopy, the sulfide crystallization order is pyrite (siegenite) → chalcopyrite → bornite → galena + sphalerite (Fig. 7i). Early-stage gypsum and barite are distributed around the pyrite-chalcopyrite, probably due to the retrograde dissolution in the later stage (Fig. 7i). This is similar to the early-stage gypsum-barite chimney shell formed by modern seafloor exhalative sedimentation.

The lead-zinc ore lenses are mainly distributed in the northeastern margin of Yushui, distal from the fluid channel. Footwall of the copper lenses comprises purplish-red quartz sandstone, while that of the lead-zinc ore lenses (1.5–6 m) comprises 1–9-m-thick bioclastic limestone. Exhalites are found above the lead-zinc ore lenses, and no alteration is present between the lead-zinc lenses and the hanging-wall (Fig. 6f). The lead-zinc lenses contain mainly pyrite, galena, sphalerite, and minor chalcopyrite (mainly in the base of lenses). The lead-zinc lenses contain mainly pyrite, galena, sphalerite, and minor chalcopyrite (mainly in the base of lenses). The lead-zinc ore lenses comprise stratiform ores (Fig. 7j), white coarse-grained hydrothermal dolomite, and exhalites in order from the footwall to the roof (Figs. 6g and 7k).

Sampling and analytical methods

Sampling

The hematite samples for U-Pb dating were separated from the massive copper ores in the middle of the deposit, whereas the dolomite samples for Sm-Nd dating were separated from the stratiform lead-zinc ores at the deposit margin (Fig. 4). The ore used for in situ U-Pb dating are hematite, chalcopyrite with minor pyrite in a brecciated structure. The hematite (size, 5 to 100 μm) is acicular or flaky, and is cemented by chalcopyrite, suggesting that the hematite was formed slightly before chalcopyrite, and its age can represent the early-stage mineralization age (Fig. 7g). The samples used for Sm-Nd dating are euhedral coarse-grained dolomite, which intergrow with galena and sphalerite, suggesting that they were formed in the same stage (Figs. 6g and 7j, k). In addition, the hydrothermal dolomite cuts chalcopyrite (Fig. 7g), suggesting that its age can represent the late-stage mineralization age.

Analytical methods

fs-LA-(MC)-ICP-MS U-Pb dating and trace element of hematite

The analyses were conducted at the State Key Laboratory of Ore Deposit Geochemistry, Institute of Geochemistry,

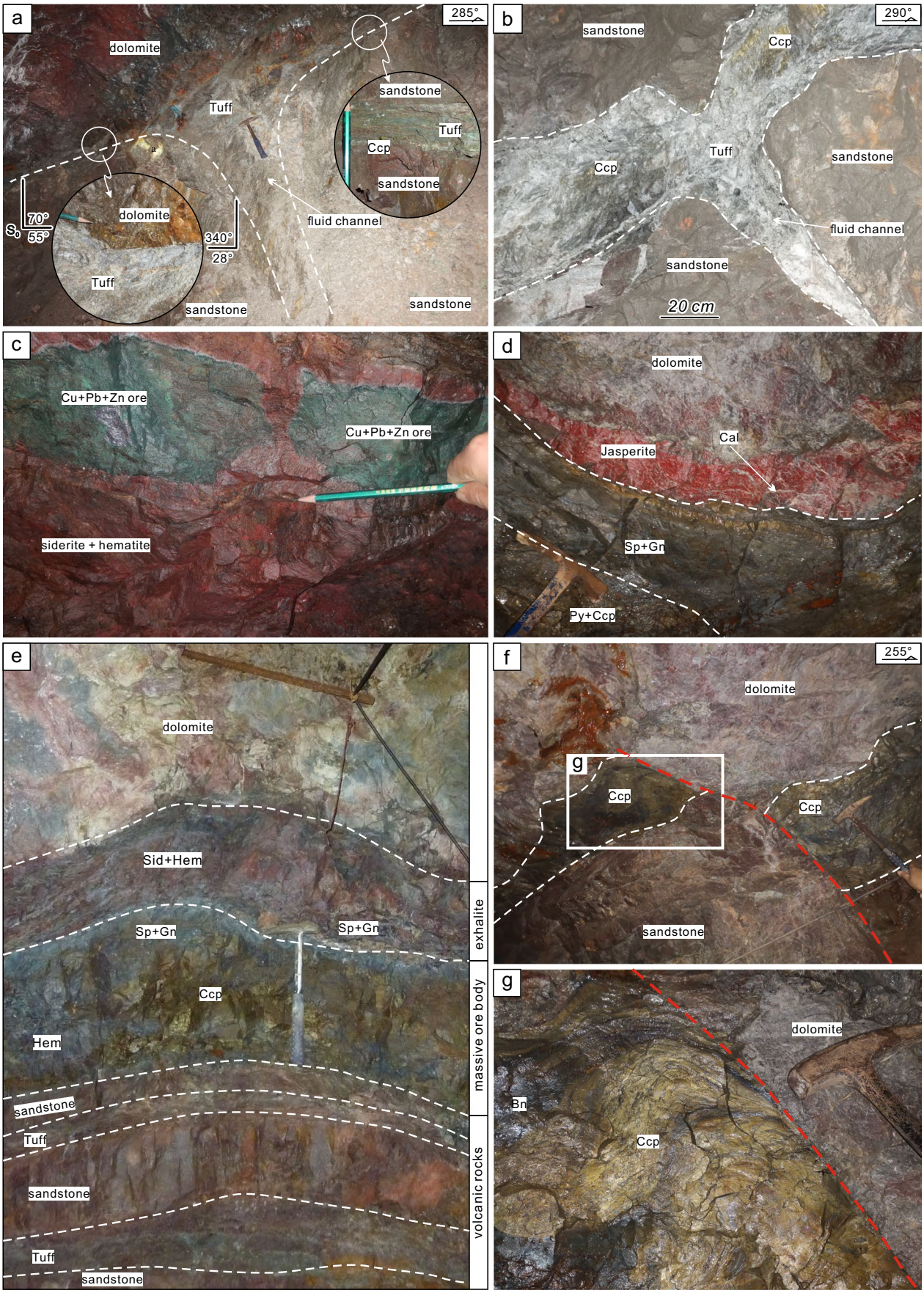
a
285°
dolomite
Tuff
sandstone
Tuff
Ccp
sandstone
fluid channel
dolomite
70°
55°
S_0
340°
28°
Tuff
sandstone
sandstone
b
290°
sandstone
Ccp
Ccp
Tuff
sandstone
fluid channel
sandstone
20 cm
c
Cu+Pb+Zn ore
Cu+Pb+Zn ore
siderite + hematite
d
dolomite
Cal
Jasperite
Sp+Gn
Py+Ccp
e
dolomite
Sid+Hem
Sp+Gn
Sp+Gn
Ccp
Hem
sandstone
Tuff
sandstone
Tuff
sandstone
exhalite
massive ore body
volcanic rocks
f
255°
dolomite
g
Ccp
Ccp
sandstone
g
dolomite
Bn
Ccp

◂**Fig. 5** Field photographs for typical features of the Yushui Cu ores. **a** Volcanic ash and volcanic channels; **b** volcanic ash–filled horn-shaped volcanic channel; **c** lenticular bedding at the pinch of orebody, and the Cu-Pb-Zn ore is distributed in the red exhalites; **d** jasperite ore underground workings with clear stratiform structure (from bottom to top): pyrite-chalcopyrite layer, galena-sphalerite layer, and red jasperite. Flame structure appears at the bottom; **e** a complete vertical section of the orebody; **f** syn-volcanic faults; **g** drag fold in syn-volcanic faults. Abbreviations: Bn, bornite; Ccp, chalcopyrite; Gn, galena; Hem, hematite; Sp, sphalerite; Sid, siderite

Chinese Academy of Sciences. Before the analysis, select the appropriate sample grinding restricted 0.1-mm-thick probe, combining with BSE hematite crystal characteristics and determination of main elements as a result, the crystal structure is good for delineating the hematite particles were analyzed. The analysis spots were chosen to avoid cracks, inclusions, or other impurities, to reduce the common Pb influence. Laser ablation used a NWR UP-213 Nd:YAG laser, and an Agilent 7700x ICP-MS instrument was used to acquire ion-signal intensities. Helium was used as the carrier gas, which was mixed with argon make-up gas via a T-connector before entering the ICP-MS. Each analysis includes a background acquisition of ~30 s (gas blank), followed by 50 s of sample data acquisition. Element contents were calibrated against multiple reference materials (GSE-1G, BCR-2G, BIR-1G, and BHVO-2G) with internal standardization (Dare et al. 2012). The recommended element concentrations for the USGS reference glasses are from the GeoReM database (http://georem.mpch-mainz.gwdg.de/). Off-line selection and integration of background and analyte signals and time-drift correction and quantitative calibration were performed with ICPMSDataCal (Liu et al. 2008, 2010). Thermo Element XR high-resolution magnetic mass spectrometry (HR-ICP-MS) and excimer laser ablation system (GeoLasPro 193nm) were used for the analysis. The analytical conditions include 32 μm beam diameter, 3J/cm^2 laser energy density, and 5 Hz frequency. Helium and Ar were used as the carrier gas (0.45 L/S) and make-up gas, respectively. Each spot analysis comprises 80 s, including 20 s background acquisition (laser-off), 25 s sample signal measurement (laser-on), and 35 s cleaning time. Analyses of the samples were bracketed by that of the standards (twice in the order of NIST SRM612, 91500, YGX, and WT). Standard zircon 91500 (1062 Ma) was used as the main correction sample. The U-Pb isochron ages were calculated using the Isoplot/Ex_V3 program (Ludwig 2003).

Dolomite geochemical and Sr and Sm-Nd isotopic analyses

Hydrothermal dolomite samples were crushed to 200 mesh for geochemical analyses. For the isotope analyses, the Sm and Nd separation was done by conventional two-column chromatography (AG50W resin column + HEHEHP resin column). The Sm-Nd isotopic analysis was performed on a Thermo Fisher Scientific Triton thermal ionization mass spectrometer (TIMS), with the analytical errors for $^{149}Sm/^{147}Sm$ and $^{146}Nd/^{145}Nd$ being lower than ±0.05%. The Sm and Nd contents and the $^{147}Sm/^{144}Nd$ value were calculated with the isotope dilution method (Rosenblum 1957). $^{143}Nd/^{144}Nd$ was corrected against $^{146}Nd/^{144}Nd$ (0.7219) for the mass fractionation correction. The JNdi-1 Nd standard yielded $^{143}Nd/^{144}Nd = 0.512116 \pm 0.000007$ (2σ) (Tanaka et al. 2000), and the international rock standard BCR-2 ($^{143}Nd/^{144}Nd = 0.512643 \pm 0.000011$; 2σ) was used to evaluate the separation and purification of Nd. Detailed instrumental parameters and separation process were described in Liu et al. (2019). The Sm-Nd isochron ages were calculated with the Isoplot/Ex_V3 program (Ludwig 2003). The Sr isotope analysis used 0.10g of the powdered sample, which was dissolved by 2.5 mol/L HCl, and the supernatant was centrifuged for resin separation. The separation and purification of Sr were conducted using AG50W×12 strong acid cation exchange resin. The interference and inhibition of ^{87}Rb on ^{87}Sr isotropy and matrix elements were minimized, ensuring high precision and accuracy of the obtained Sr isotope ratios. The international JDo-1 carbonate standard (dolomite, purchased from GSJ, Japan) was used to monitor the separation process. Our analysis yielded $^{87}Sr/^{86}Sr = 0.707572 \pm 0.000008$(2SE), and the internal correction factor for Sr fractionation ($^{88}Sr/^{86}Sr$) is 8.375209. Isotope ratios were determined on a Triton TIMS using ion sources with parallel double filament components. The international BCR-2 Sr standard yielded $^{87}Sr/^{86}Sr = 0.705024 \pm 0.000007$ (2SE). The use of laboratory resin and its separation process followed those described by Liu et al. (2019).

Results

Hematite U-Pb age and trace element compositions

The LA-ICP-MS isotope signals for many elements, including ^{238}U, ^{206}Pb, ^{207}Pb, ^{202}Hg, ^{204}Pb, and ^{232}Th, are generally stable across the 40-s signal acquisition area. Uranium of hematite is mainly hosted in the mineral lattice, and thus the U-Pb age can represent the hematite formation age.

A total of 65 U-Pb isotope spot analyses were conducted on sample YS3-10, and 55 sets of valid data were obtained (the rest likely contaminated by fine inclusions or impurities in fissures). The hematite has 0 to 0.06 ppm (average 0.01 ppm) Th, 4.45 to 35.54 ppm (average 15.37 ppm) U, and 2.56 to 369.61 ppm (average 70.30 ppm) Pb. The samples have $^{207}Pb/^{206}Pb = 0.86$ to 0.32, $^{207}Pb/^{235}U = 3.35$ to 282.57, and $^{206}Pb/^{238}U = 0.07$ to 2.40 (ESM 2B). Due to the high common Pb content, the T-W inverse concordia plot was

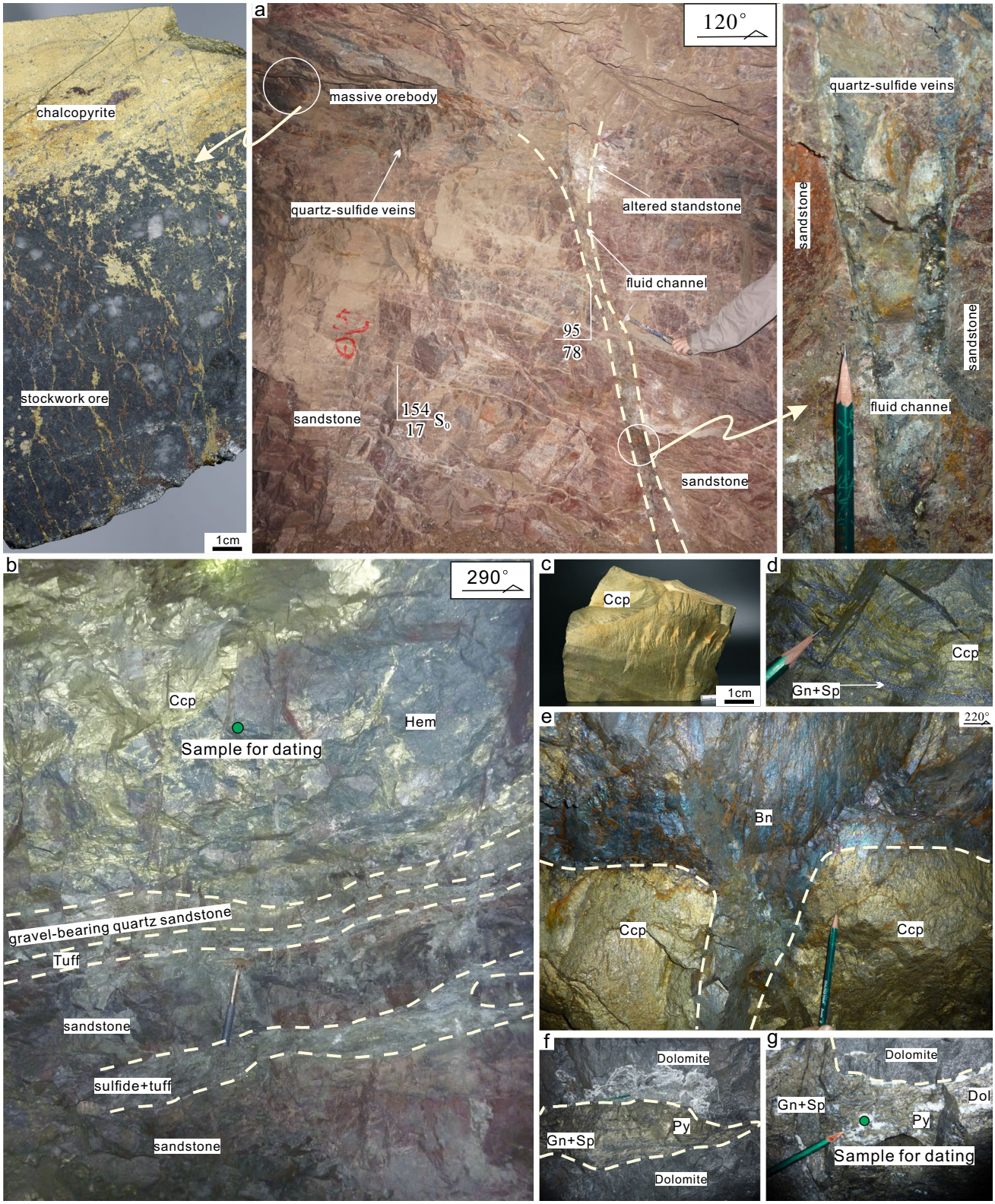

Fig. 6 Field and hand-specimen photographs of the Yushui copper deposit. **a** Hydrothermal system with a main fluid channel and fan-shaped sulfide quartz stringer on its sides; **b** two tuff layers in quartz sandstone, and chalcopyrite-hematite at the base of the stratiform orebody; **c** massive chalcopyrite ore; **d** ribbon-/banded-ore with pyrite, chalcopyrite, galena, and sphalerite; **e** large funnel-shaped bornite orebody; **f** interfinger contact relation between orebody and unaltered dolomite; **g** hydrothermal dolomite in orebodies. Abbreviations: Bn, bornite; Ccp, chalcopyrite; Gn, galena; Py, pyrite; Sp, sphalerite

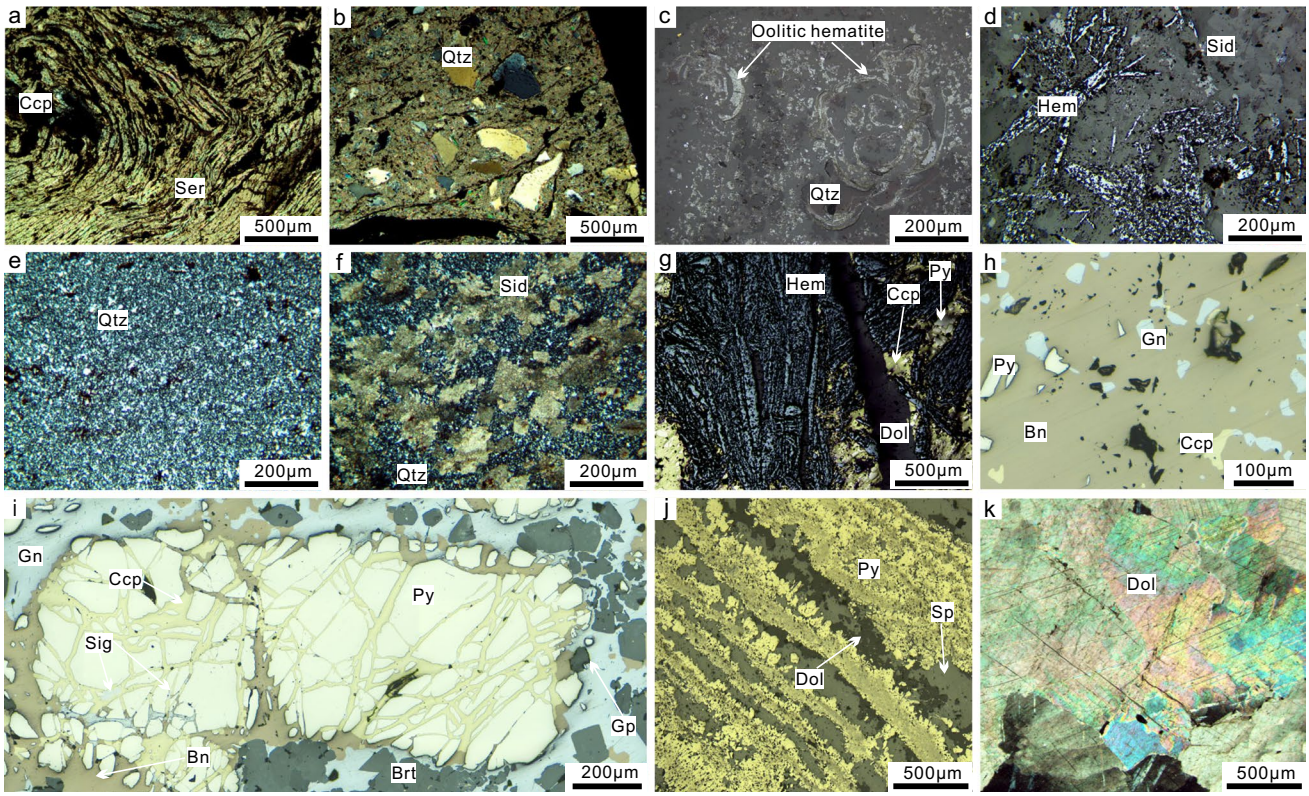

Fig. 7 Microphotographs of typical ore textures in the Yushui copper deposit. **a** Sericite and chalcopyrite in volcanic rocks (crossed-polar); **b** quartz crystal fragments in tuff (crossed-polar); **c** oolitic hematite in exhalites (reflected light); **d** siderite and hematite coexist (reflected light); **e** jasperite is composed of fine-grained quartz (crossed-polar); **f** fine-grained quartz coexists with siderite (crossed-polar); **g** pyrite-chalcopyrite-cemented hematite (reflected light); **h** micro-structure of bornite (reflected light); **i** breccia structures showing the mineral crystallization sequence: pyrite → chalcopyrite → bornite → sphalerite and galena; **h** gypsum in galena (reflected light); **j** lamellar interbedded pyrite and sphalerite (reflected light); **k** coarse-grained hydrothermal dolomite (crossed-polar). Abbreviations: Bn, bornite; Brt, barite; Ccp, chalcopyrite; Dol, dolomite; Gn, galena; Gp, gypsum; Py, pyrite; Sp, sphalerite; Sig, siegenite; Sid, siderite; Te, tetrahedrite

used for common Pb correction, yielding a lower intercept age of 320 ± 15 Ma (MSWD = 2.1, n = 57) (Fig. 8).

Hematite geochemical compositions of sample YS3-10 (20 spots) were measured, and the analysis results are listed in ESM 2E and illustrated in ESM 3-4 and Fig 10. The sample has total Fe content of 93.7 to 96.8 wt%, together with minor Si, Ti, Al, and V, as well as trace Co, Ni, Cu, Zn, Ga, Ge, As, Y, Mo, Ag, Cd, In, Sn, Sb, Te, Ho, W, Tl, Pb, Bi, Pb, and U. Meanwhile, concentrations of Au, Se, and Te are below the detection limit. The YS3-10 hematite grains are significantly metal rich, including V (1886.8–16495.4 ppm, average 9300 ppm), Ni (average 334 ppm), Ga (average 183 ppm), and Pb (average 352.4 ppm). The Ag, Cd, Tl, and Bi contents are generally below 1 ppm (ESM 2E, 3).

Dolomite Sr and Sm-Nd isotope compositions

The Sr-Sm-Nd elemental and isotopic compositions of the Yushui dolomite samples are shown in ESM 2C. The samples (n = 7) have 0.0950 to 10.2471 ppm Sm and 0.2542 to 50.5161 ppm Nd, with $^{147}Sm/^{144}Nd$ = 0.1030 to 0.2962

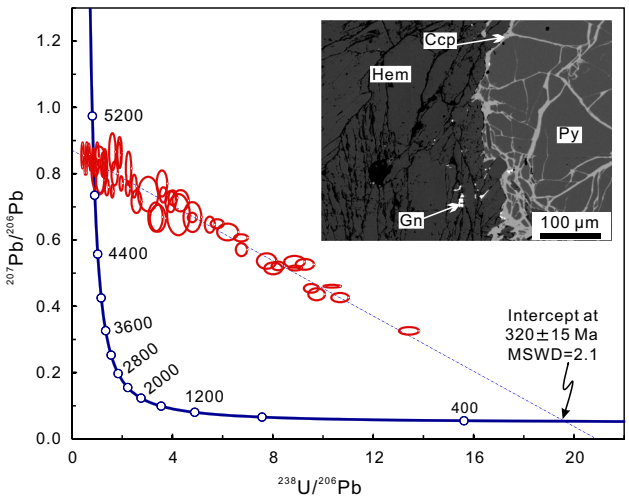

Fig. 8 $^{207}Pb/^{206}Pb$-$^{238}U/^{206}Pb$ isochron plot of hematite from the Yushui copper deposit

and $^{143}Nd/^{144}Nd = 0.511825$ to 0.512207, yielding a Sm-Nd isochrones (t = 308.1 ± 4.6 Ma; n = 7; MSWD = 0.94; initial $^{143}Nd/^{144}Nd = 0.5116186$) (Fig. 9). The dolomite has $\varepsilon Nd(0) = -15.86$ to -8.41, $\varepsilon Nd(t) = -12.64$ to -11.97, and t_{DM2} = 2042 to 2134 Ma. The hydrothermal dolomite has $^{87}Sr/^{86}Sr = 0.711847$ to 0.715072 (average 0.713745), representing the ore-fluid Sr isotopic compositions.

Discussion

Mineralization age

With ongoing advancements in LA-ICP-MS technology, hematite U-Pb dating has has demonstrated its reliability, much like monazite, apatite, and fluorocerium (Ciobanu et al. 2013; Courtney-Davies et al. 2016, 2019; Apukhtina et al. 2017; Zhou et al. 2017). Hematite and magnetite are widespread in various hydrothermal deposits, including porphyry, skarn, iron oxide-copper-gold (IOCG), and VMS deposits (Zhou et al. 2017; Meinert et al. 2005; Chen et al. 2010; Franklin et al. 2005). Previously, hematite U-Pb dating is mostly applied to IOCG and porphyry gold deposits (Ciobanu et al. 2013; Courtney-Davies et al. 2016; Apukhtina et al. 2017; Zhou et al. 2017; Verdugo-Ihl et al. 2022), and was considered only suitable for old hematite samples due to the lack of suitable hematite standard (Courtney-Davies et al. 2020). However, recent studies have confirmed its applicability for young samples as well (Zhou et al. 2017; Verdugo-Ihl et al. 2022), and have demonstrated that 91500 and GJ-1 zircon standard can help mitigate matrix effects (Courtney-Davies et al. 2016, 2020; Zhou et al. 2017).

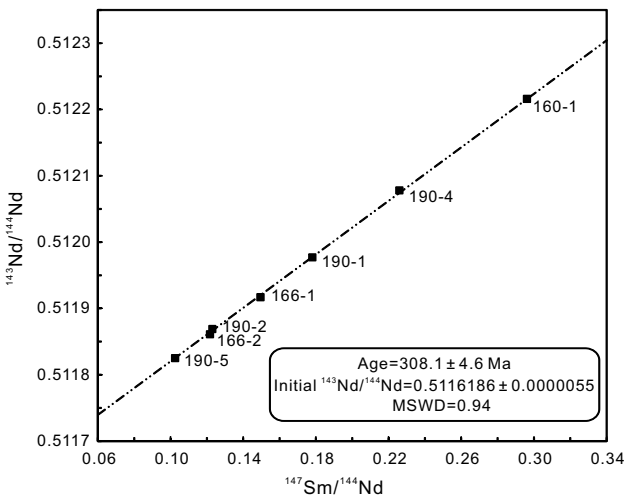

Fig. 9 $^{143}Nd/^{144}Nd$ vs. $^{147}Sm/^{144}Nd$ isochron diagram for seven dolomite samples

Both samarium (Sm) and neodymium (Nd) are rare earth elements (REEs). The Sm-Nd isotope system is unaffected by magma fractionation or moderate alteration/weathering, and can be used for dating (Hamilton et al. 1977, 1979). Hydrothermal carbonate Sm-Nd dating has been successfully employed in various deposit types, including SEDEX, Carlin-type, REE, and hydrothermal vein-type deposits, yielding reliable dates (Fryer and Taylor 1984; Nie et al. 1999; Jiang et al. 1999, 2000; Kempe et al. 2001; Peng et al. 2003; Su et al. 2009; Sánchez et al. 2010; Fan et al. 2014; Maas et al. 2022).

Our obtained hematite U-Pb (320 ± 15 Ma) and hydrothermal dolomite Sm-Nd (308.1 ± 4.6 Ma) dates are consistent (within error) with the published Re-Os age (308 ± 15 Ma) of chalcopyrite and bornite in the massive sulfide lenses (Huang et al. 2015a, b). Furthermore, the formation age (320 to 308.1 Ma) of hematite in the early-stage mineralization and late-stage hydrothermal dolomite also conform to the established mineral paragenetic sequence. These hydrothermal mineralization ages are coeval with the formation ages of the Zhongxin and Hutian Formation host rocks (Fig. 3), indicating that the Yushui copper mineralization is syngenetic and occurred in the Carboniferous. This supports the conclusion that Yushui is not an epigenetic deposit, as previously suggested, such as a MVT or late-stage hydrothermal replacement deposit (Chen et al. 1994; Cai and Liu 1996; Liu 1997; Cheng et al. 2014).

Deposit type

Similar massive sulfide deposits were developed in the late Paleozoic South China, and all the orebodies were hosted in the clastic-carbonate lithological contact (Gu et al. 2007). Our dating results (ESM 2D) support that the stratiform sulfide orebodies are of seafloor exhalative sedimentary origin. This indicates probable widespread exhalative sedimentary mineralization in late Paleozoic (esp. Carboniferous) South China.

Syngenetic massive sulfide deposits are generally classified as SEDEX and VMS, the major difference between which is whether they are volcanic-related. In this study, we confirm that ore-related volcanic rocks are present at Yushui (Fig. 5a, b). The two volcanic layers at Yushui are mafic, which resemble mafic-siliciclastic-type VMS deposits in terms of their host-rock characteristics and Cu-rich nature (Barrie and Hannington 1999). Mafic-siliciclastic-type VMS deposits are generally associated with continental rifts (Pirajno and Cawood 2009; Pirajno et al. 2016), and the Yushui was likely formed in a rift basin (Fig. 1).

Huang (2015) classified the Yushui copper deposit as SEDEX, but the S isotope has both volcanic and seawater sources, and the Pb isotope also indicates that the ore-forming material was originated from the mixing of crust and mantle, which is different to typical SEDEX deposits. The

geological features (incl. volcanic host rock, exhalites, lower string zone and upper massive zone, syn-volcanic faults), mineralization age of this study, and published geochemical data (S-Pb-Cu-Fe-C-H-O isotopes and fluid inclusions feature; Huang 2015; Wang et al. 1999) further support that the Yushui deposit belong to VMS type.

Hematite is a homogenous polymorph of magnetite, and inherits many properties of magnetite (Dupuis and Beaudoin 2011; Huang et al. 2015a, b, 2019b). Hematite and magnetite can be interconverted under various physical and chemical conditions. The trace elements of hematite can indicate the same physical and chemical conditions as magnetite (Matthews 1976; Ohmoto 2003; Otake et al. 2010). Geochemical compositions of hematite can be used to constrain the physicochemical conditions of ore-forming fluids, and to distinguish deposit types, including IOCG, iron oxide-apatite (IOA), band iron formation (BIF), porphyry, skarn, magmatic Fe-Ti oxide and Cu-Ni-PGE, and VMS (Boutroy et al. 2014; Dare et al. 2014; Sappin et al. 2014; Makvandi et al. 2016; Huang et al. 2019a).

Hematite samples from Yushui exhibit notably high vanadium (V) content, reaching up to 10,000 ppm (ESM 3). Such ultra-high V content is a rarity and has only been observed in a few VMS deposits globally, including the Red Sea (9860 ppm), the Dahongshan copper deposit (11,459 ppm), and some iron deposits in Northwest China (8269 ppm) (Jedwab et al. 1989; Zhou et al. 2017; Wang et al. 2020). The ultra-high V content indicates that the Yushui hematite share similar deposition environment with hematite from the Red Sea.

Because magmatic and hydrothermal magnetite have different iron contents, Wen et al. (2017) proposed the Fe vs. V/Ti plot to determine the magnetite origin. The Yushui hematite has high Fe and high V/Ti contents (ESM 2E), and fall into the hydrothermal field (Fig. 10a). In addition, in the

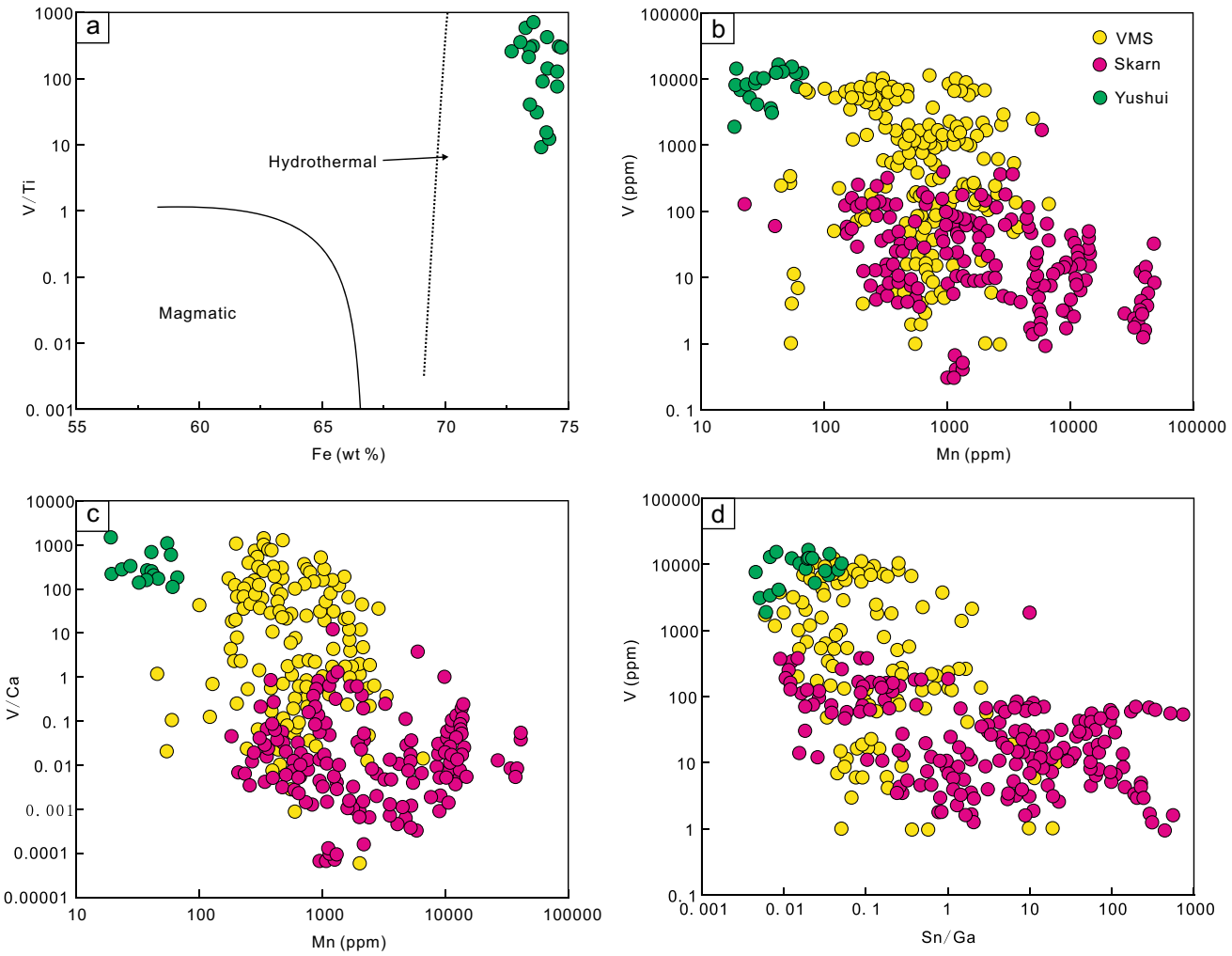

Fig. 10 (**a**) V/Ti vs. Fe discrimination plot (Wen et al. 2017), and binary plots of **b** V vs. Mn, **c** V/Ca vs. Mn, and **d** V vs. Sn/Ga for the Yushui hematite. Data source: VMS deposits from Makvandi et al. (2016); skarn deposits from Zhao and Zhou (2015), Hu et al. (2017), Ding et al. (2018), Li et al. (2018), Chen et al. (2020, 2021), Dong et al. (2021), Peng et al. (2021), and Xing et al. (2022)

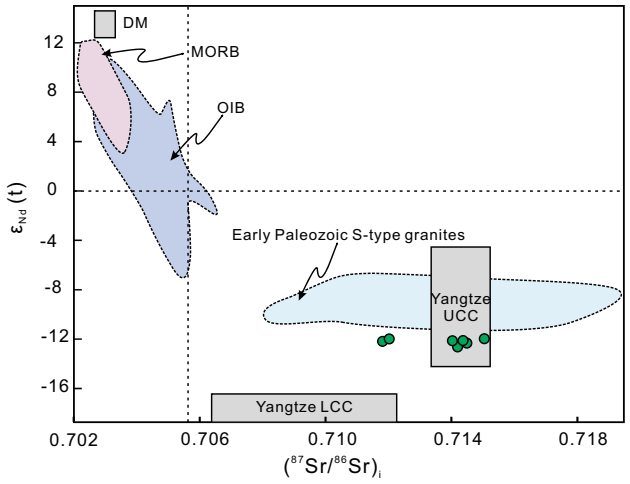

Fig. 11 ($^{87}Sr/^{86}Sr$)i vs. ε_{Nd} diagram showing compositional variations of the Yushui dolomite. Initial isotope ratios are corrected to 308 Ma, and the MORB and OIB fields are from Zindler and Hart (1986). The Yangtze lower continental crust (LCC) and the Yangtze upper continental crust (UCC) fields are from Zhao et al. (2010) and Hao (1993), respectively. Green dots represent the Yushui copper deposit

Mn vs. V, Sn/Ga vs. V, and Mn vs. V/Ca plots (Fig. 10b–d), all our hematite samples fall into the VMS field. Hence, we argued that Yushui is of VMS type, instead of skarn type or other hydrothermal types (Makvandi et al. 2016). To further constrain the hematite origin from Yushui, we compared it with the hematite from typical skarn and VMS deposits worldwide. The Yushui hematite contains significantly lower Ca and Mn than VMS (ESM 4a-b), but higher Ga and V than VMS (ESM 4c-d). In particular, the content of V and Ca is highly comparable to the VMS-type magnetite. The concentration ranges and median values of Mn and V are also largely similar to those of the VMS-type magnetite, but distinctly from those of the skarn-type magnetite (ESM 4).

While Yushui copper deposit shares many characteristics with VMS deposits, one might still challenge the idea of the shallow water depositional environment represented by its host rock. In fact, there are many shallow marine SMS and VMS examples around the world, such as those that (1) show characteristics of carbonate host rock deposits, e.g., Kidd Creek, Southern orebody of the Iberian Pyrite Belt, and the Ambler district (NW Alaska) (Hitzman et al. 1986; Taylor and Huston 1999; Tornos 2006); (2) formed in shallow marine volcanic depressions, e.g., Panarea, Aeolian Island Arc (Italy) (Marani et al. 1997; Dekov et al. 2013), the Lake Tanganyika (East African Rift) (Tiercelin et al. 1993), and the Afar Rift (eastern Ethiopia) (Bonatti et al. 1972), the hydrothermal activity found about 100 km north of Iceland (Fricke et al. 1989; Olafsson et al. 1989; Botz et al. 1999), and the Salton Sea (Southern California) (Arango-Galván et al. 2011).

Studies on the abovementioned deposits confirmed that in the early rifting stage of mid-ocean ridges, or at where the ocean ridges extend landward, hydrothermal activity and sulfide accumulation could occur in shallow marine environment (water depth: 0–1000 m) (Wilson and Rocha 1955; Elders 1979; Olafsson et al. 1989; Shanks and Callender 1992). Thin tuff-dominated volcanic layers are the common features of these shallow marine sulfide deposits (Monecke et al. 2014). Therefore, modern seafloor hydrothermal mineralization can occur at different water depths (0–5200 m), and they are all closely related to seafloor spreading and rifting activities (Franklin et al. 2005; Hannington et al. 2005).

We suggest that the Yushui is a VMS deposit formed in shallow marine environment, with different genesis compared to the typical (deep water) VMS deposit. Goodfellow et al. (2003) identified a type of VMS with sedimentary-hosted deposit, including the Bathurst district (Canada), Iberian Pyrite Belt (Spain), Wolverine (Yukon, Canada), and Xitieshan (China) (Fu et al. 2017).

Genesis of the Yushui deposit and its exploration implications

Calcite Sr-Nd isotopes have been widely used to determine the source of ore-forming fluids and minerals (Hecht et al. 1999; Barrat et al. 2000). Our samples exhibit $^{87}Sr/^{86}Sr$ values ranging from 0.715072 to 0.711847, with an average of 0.713737 (ESM 2C). In contrast, the $^{87}Sr/^{86}Sr$ range for Carboniferous seawater in Southwestern Fujian falls between 0.7080 and 0.7084 (Chen et al. 2018). There is no obvious Sr isotope fractionation during the marine carbonate diagenesis, and carbonate Sr isotope compositions are close to that of contemporaneous seawater (Veizer 1989, 1999). The $^{87}Sr/^{86}Sr$ value of the hydrothermal dolomite in this study differs significantly from that of the host rock sample (contemporaneous carbonate). Since Rb decays into ^{87}Sr during rock weathering, this would lead to higher $^{87}Sr/^{86}Sr$ value in more-matured crustal source material. The $^{87}Sr/^{86}Sr$ of hydrothermal dolomite is significantly higher than that of seawater and global mantle source $^{87}Sr/^{86}Sr$ (0.7035), but lower than that of global crustal source $^{87}Sr/^{86}Sr$ (0.71190) (Palmer and Edmond 1989). Therefore, the Sr of hydrothermal dolomite in the Yushui ore-forming hydrothermal fluid is likely to be contaminated by highly matured crustal materials.

In the $\varepsilon_{Nd}(t)$ vs. $^{87}Sr/^{86}Sr$ diagram, all data fall within the early Paleozoic S-type granite field (Fig. 11). Combined with the previous studies on the ore element abundance of local pre-Devonian strata (which show high background contents of Cu, Pb, Zn, and Ag) (Cai and Liu 1996), we propose that the metallogenic materials primarily originated from the crustal basement. This conclusion is consistent with that drawn from siliceous clastic-dominated VMS deposits in the Iberian Pyrite Belt (Tornos 2006).

Many lithofacies paleogeographic studies suggested that the Late Carboniferous Yushui was in a terrestrial-marine transition (under extensional tectonics) with epicontinental sea sedimentation (Fig. 12a) (Zhao et al. 1996; Wang and Jin 2000; Cai and Zhang 2009; Wang et al. 2017), and that the Paleo-Japan Arc was related to South China. According to tectonic model, the eastern South China was positioned in a distal continental back-arc extension setting (Fig. 12b) (Cocks and Torsvik 2013; Domeier and Torsvik 2014; Isozaki et al. 2010). This is supported by the presence of coeval extension-related (e.g., bimodal) magmatic units in the region (Wang 2005; Hu et al. 2012, 2015; Shen et al. 2018; Wang et al. 2017; Gao et al. 2022).

Hydrothermal fluids may have leached the ore metals from the metal-rich crustal basement at Yushui (Huang et al. 2015a, b). Previous studies suggest that the mineralization temperature at Yushui is low (110–220 ℃) (Cheng et al. 2014), which is contradictory to the high precipitation temperature required for copper sulfides. However, the hydrothermal leaching model demonstrated that basinal brine in the low-temperature phase is injected in batches that produced phase separation of high-temperature copper-rich fluids, which accounts for the copper enrichment in the lower part of the Yushui deposit (Ohmoto 1996; Hannington et al. 1999b-c; Tornos and Spiro 1997, 1999; Tornos 2006). In essence, the Late Carboniferous regional extension may have caused enhanced heat flow and fluid convection in the crustal basement, which contributed to the Yushui copper mineralization in a shallow marine rift (Fig. 12c).

According to the mineralization control of the rift basin and the principle of fault equidistance (Sangster 1980), similar deposits could potentially form in the upper Paleozoic Yong'an-Meizhou-Huizhou depression. In fact, there are numerous examples of massive deposits within the other

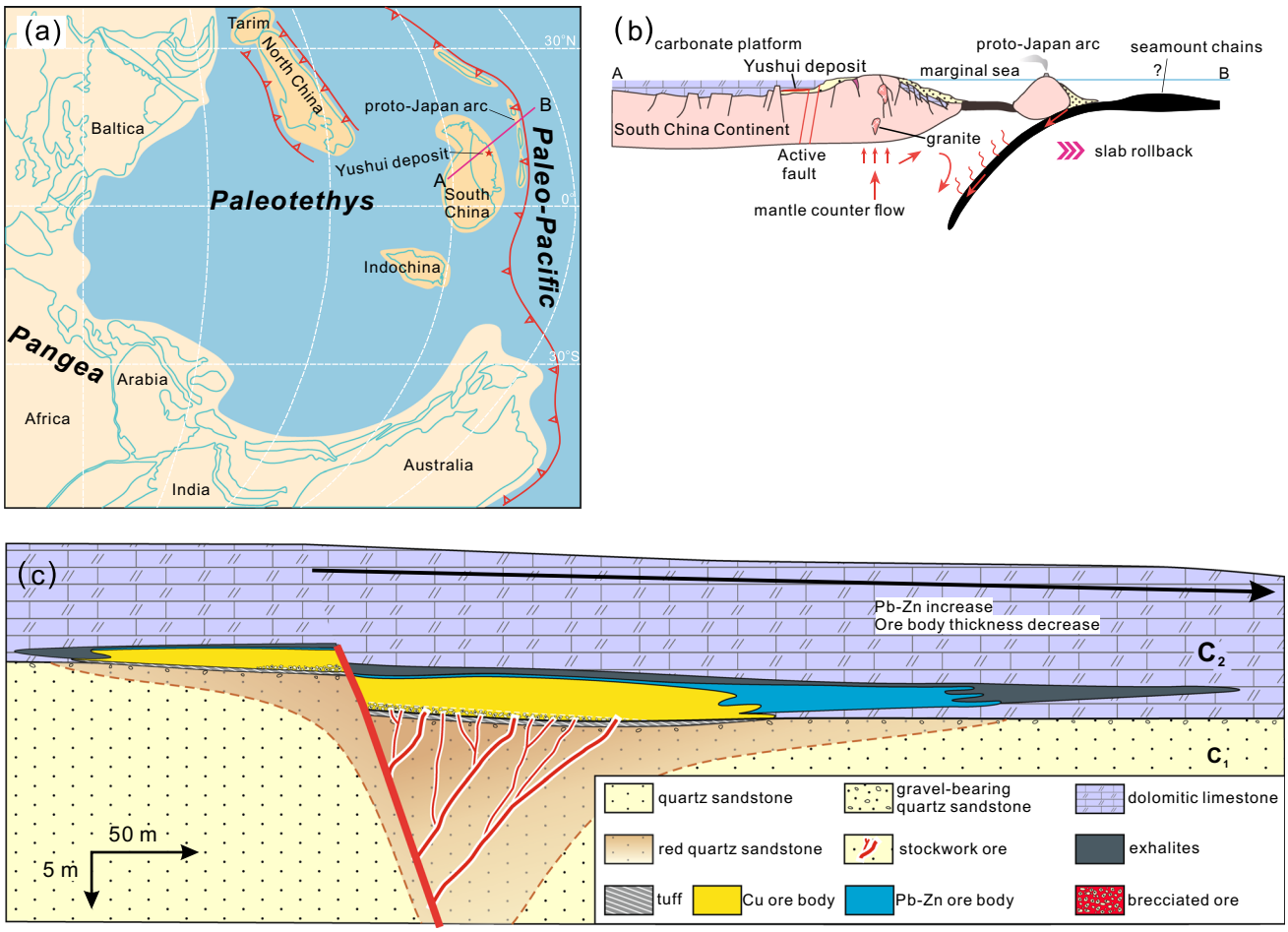

Fig. 12 Late Carboniferous paleogeographic map **a**, and the corresponding schematic cross section **b**, illustrating that the eastern South China changed from a distal continental back-arc to an active continental margin setting by the Proto-Japan island arc accretion. Map modified after Isozaki et al. (2010), Cocks and Torsvik (2013), Metcalfe (2013), and Domeier and Torsvik (2014); **c** schematic metallogenic model for the Yushui copper deposit (modified from Chen et al. 2021)

depressional zone in the same period, e.g., the Wushan and Chengmenshan (Gu et al. 2007; Jiang et al. 2010; Kong et al. 2012), Yongping (Gu et al. 2007), and the Xinqiao and Dongguashan (Xie et al. 1995; Guo et al. 2011; Jiang et al. 2011) copper deposits. The stratigraphic age should be given priority in the exploration of VMS deposits (Gibson 2007; Galley et al. 2007), i.e., the interface between the upper Carboniferous carbonate rocks and the lower Carboniferous quartz sandstone is the predicted target horizon. The second priority is the near NS or NNE-trending fault due to the consideration of fluid channels and the production of syn-volcanic faults are in this direction (Figs. 5f and 6a). Ridler (1971) defined exhalites as chemical sedimentary rocks formed by hydrothermal fluids venting. Based on lithological and geochemical data, exhalites are broadly considered as amorphous Fe ± Mn ± Si ± S ± Ba ± B phases precipitated from seafloor hydrothermal vents and plumes with a wide lateral spread (Kimberley 1989; Isley 1995; Peter 2003; Grenne and Slack 2005). The large-scale red exhalites found at the roof of Yushui copper deposit can also serve as a valuable regional prospecting indicator, following a precedent set in the world (Aggarwal and Nesbitt 1984; Spry and Peter 2000; Peter 2003; Galley et al. 2007; Chen et al. 2015). Furthermore, the presence of disseminated chalcopyrite and pyrite mineralization, along with volcanic rock interlayers in the sandstone at the base of the orebody, can serve as essential criteria for peripheral prospecting and the delineation of regional massive sulfide ore prospecting targets.

Conclusions

In this study, we identify geological evidence of syn-volcanic faults, exhalites, and double-layered mineralization at the Yushui copper deposit. The hematite is V-rich and likely of submarine hydrothermal origin, similar to that from the Red Sea. The ore-forming materials were likely originated from the basement, and the mineralization age (308–320 Ma) is coeval with the Upper Carboniferous wallrocks. Accordingly, we argued that the Yushui is a shallow marine VMS deposit.

Supplementary Information The online version contains supplementary material available at https://doi.org/10.1007/s00126-023-01232-5.

Acknowledgements Editors-in-Chief Bernd Lehmann, associate editor Shao-Yong Jiang, and one reviewer are thanked for the constructive reviews that greatly improved the quality of this paper. We thank Dr. Yongfei Tian, Kezhong Ma and local geological Mr. Wei Zhang and Yongxin Peng for helping with the field investigation. Our thanks also go to Profs. Jingwen Mao, Bernd Lehmann, Larry Meinert, and Richard Goldfarb for their guidance and comments during the field trips to the Yushui copper deposit. We are grateful to Profs. Zhenyu Chen, Zhihui Dai, and Wengang Liu for helping with the data collection; to Profs. Tornos Fernando, Fuquan Yang, and Dr. Wenhao Tang for their suggestions on the manuscript draft; and to Dr. Junzeng Zuo, Zhiqiang Zhang and Sean McClenaghan for polishing up the language of this manuscript.

Funding This research was funded by the National Natural Sciences Foundation of China (42072110) and the China Geological Survey mineral survey project (DD20201173).

Declarations

Competing interests The authors declare no competing interests.

References

Aggarwal PK, Nesbitt BE (1984) Geology and geochemistry of the Chu Chua massive sulfide deposit, British Columbia. Econ Geol 79:815–825. https://doi.org/10.2113/gsecongeo.79.5.815

Apukhtina OB, Kamenetsky VS, Ehrig K, Kamenetsky MB, Maas R, Thompson J, McPhie J, Ciobanu CL, Cook NJ (2017) Early, deep magnetite-fluorapatite mineralization at the Olympic Dam Cu-U-Au-Ag deposit, South Australia*. Econ Geol 112:1531–1542. https://doi.org/10.5382/econgeo.2017.4520

Arango-Galván C, Prol-Ledesma RM, Flores-Márquez EL, Canet C, Villanueva Estrada RE (2011) Shallow submarine and subaerial, low-enthalpy hydrothermal manifestations in Punta Banda, Baja California, Mexico: geophysical and geochemical characterization. Geothermics 40:102–111. https://doi.org/10.1016/j.geothermics.2011.03.002

Baker ET (2004) German CRJM-ORHIBtL, Oceans GMS. On the global distribution of hydrothermal vent fields. 148:245–266

Barrat JA, Boulègue J, Tiercelin JJ, Lesourd M (2000) Strontium isotopes and rare-earth element geochemistry of hydrothermal carbonate deposits from Lake Tanganyika, East Africa. Geochimica et Cosmochimica Acta 64:287–298. https://doi.org/10.1016/S0016-7037(99)00294-X

Barrie CT, Hannington MD (1999) Classification of volcanic-associated massive sulfide deposits based on host-rock composition. Econ Geol

Bonatti E, Fisher DE, Joensuu O, Rydell HS, Beyth M (1972) Iron-manganese-barium deposit from the northern Afar Rift (Ethiopia). Econ Geol 67:717–730. https://doi.org/10.2113/gsecongeo.67.6.717

Botz R, Winckler G, Bayer R, Schmitt M, Schmidt M, Garbe-Schönberg D, Stoffers P, Kristjansson JK (1999) Origin of trace gases in submarine hydrothermal vents of the Kolbeinsey Ridge, north Iceland. Earth Planet Sci Lett 171:83–93. https://doi.org/10.1016/s0012-821x(99)00128-4

Boutroy E, Dare SAS, Beaudoin G, Barnes SJ, Lightfoot PC (2014) Magnetite composition in Ni-Cu-PGE deposits worldwide: application to mineral exploration. J Geochem Explor 145:64–81. https://doi.org/10.1016/j.gexplo.2014.05.010

Bureau of Geology and Mineral Resource of Guangdong (1988) Regional geology of Guangdong Province. Beijing: Geological Publishing House, 795-825(in chinese)

Cai JH, Liu JQ (1996) Characteristics of structures and prospecting targets in the metallogenic province at the south sector of Yongmei depression, Guangdong. Geotectonica et Metallogenia 4:333–339 (in Chinese with English abstract)

Cai JX, Zhang KJ (2009) A new model for the Indochina and South China collision during the Late Permian to the Middle Triassic. Tectonophysics 467:35–43. https://doi.org/10.1016/j.tecto.2008.12.003

Camprubí A, Canet C, Rodríguez-Díaz AA, Prol-Ledesma RM, Blanco-Florido D, Villanueva RE, López-Sánchez A (2007) Geology, ore deposits and hydrothermal venting in Bahía Concepción, Baja California Sur, Mexico. Island Arc 17:6–25. https://doi.org/10.1111/j.1440-1738.2007.00586.x

Canet C, Prol-Ledesma RM, Proenza JA, Rubio-Ramos MA, Forrest MJ, Torres-Vera MA, Rodríguez-Díaz AA (2005) Mn–Ba–Hg mineralization at shallow submarine hydrothermal vents in Bahía Concepción, Baja California Sur, Mexico. Chemical Geology 224:96–112. https://doi.org/10.1016/j.chemgeo.2005.07.023

Cathles LM (2010) What processes at mid-ocean ridges tell us about volcanogenic massive sulfide deposits. Mineralium Deposita 46:639–657. https://doi.org/10.1007/s00126-010-0292-9

Chen BH, Guo R, Yu SY (1994) Metallogenic features and genesis of Cu-polymetallic deposit of Yushui field Guangdong. Geol Explor 3:20–25 (in Chinese with English abstract)

Chen H, Clark AH, Kyser TK, Ullrich TD, Baxter R, Chen Y, Moody TC (2010) Evolution of the giant Marcona-Mina Justa iron oxide-copper-gold district, south-central Peru. Econ Geol 105:155–185. https://doi.org/10.2113/gsecongeo.105.1.155

Chen H, Ni P, Wang RC, Wang GG, Zhao KD, Ding JY, Zhao C, Cai YT, Xu YF (2015) A combined fluid inclusion and S-Pb isotope study of the Neoproterozoic Pingshui volcanogenic massive sulfide Cu–Zn deposit, Southeast China. Ore Geol Rev 66:388–402. https://doi.org/10.1016/j.oregeorev.2014.11.002

Chen J, Montañez IP, Qi Y, Shen S, Wang X (2018) Strontium and carbon isotopic evidence for decoupling of pCO2 from continental weathering at the apex of the late Paleozoic glaciation. Geology 46:395–398. https://doi.org/10.1130/g40093.1

Chen F, Deng J, Wang Q, Huizenga JM, Li G, Gu Y (2020) LA-ICP-MS trace element analysis of magnetite and pyrite from the Hetaoping Fe-Zn-Pb skarn deposit in Baoshan block, SW China: Implications for ore-forming processes. Ore Geol Rev 117. https://doi.org/10.1016/j.oregeorev.2020.103309

Chen MH, Ke CH, Tian YF, Chen G, Ma KZ, Ma SX, Peng YX, Zhang W (2021) Sedimentary-exhalative massive sulfide deposits in shallow marine environment, a case study Yushui copper deposit Guangdong Province. Acta Geologica Sinica 95(06):1774–1791. https://doi.org/10.19762/j.cnki.dizhixuebao.2021149

Chen G, Chen M, Ke C, Tang Y (2023) Paleozoic VMS-type stratiform mineralization overprinted by Mesozoic vein-type mineralization in the Yushui copper deposit, Eastern Guangdong. South China. Ore Geol Rev 158:105498. https://doi.org/10.1016/j.oregeorev.2023.105498

Cheng XY, Zhu XY, Wang YL, Wang H, Jiang BB (2014) Discussion on the genesis of Yushui Cu-polymetallic mineral deposits in Meizhou Guangdong. Miner Depos 33(S1):373–374 (in Chinese with English abstract)

Cherkashov G (2011) Seafloor massive sulfide deposits discovered at the Mid-Atlantic Ridge - potential target for the ocean mining in the area. OCEANS'11 MTS/IEEE KONA. https://doi.org/10.23919/oceans.2011.6106978.

Ciobanu CL, Wade BP, Cook NJ, Schmidt Mumm A, Giles D (2013) Uranium-bearing hematite from the Olympic Dam Cu–U–Au deposit, South Australia: a geochemical tracer and reconnaissance Pb–Pb geochronometer. Precambr Res 238:129–147. https://doi.org/10.1016/j.precamres.2013.10.007

Cocks LRM, Torsvik TH (2013) The dynamic evolution of the Palaeozoic geography of eastern Asia. Earth-Science Rev 117:40–79. https://doi.org/10.1016/j.earscirev.2012.12.001

Courtney-Davies L, Zhu Z, Ciobanu C, Wade B, Cook N, Ehrig K, Cabral A, Kennedy A (2016) Matrix-matched iron-oxide laser ablation ICP-MS U–Pb geochronology using mixed solution standards. Minerals 6. https://doi.org/10.3390/min6030085

Courtney-Davies L, Tapster SR, Ciobanu CL, Cook NJ, Verdugo-Ihl MR, Ehrig KJ, Kennedy AK, Gilbert SE, Condon DJ, Wade BP (2019) A multi-technique evaluation of hydrothermal hematite U Pb isotope systematics: implications for ore deposit geochronology. Chem Geol 513:54–72. https://doi.org/10.1016/j.chemgeo.2019.03.005

Courtney-Davies L, Ciobanu CL, Tapster SR, Cook NJ, Ehrig K, Crowley JL, Verdugo-Ihl MR, Wade BP, Condon DJ (2020) Opening the magmatic-hydrothermal window: high-precision U-Pb geochronology of the Mesoproterozoic Olympic Dam Cu-U-Au-Ag deposit, South Australia. Econ Geol 115:1855–1870. https://doi.org/10.5382/econgeo.4772

Crane K, Hecker B, Golubev V (1991) Heat flow and hydrothermal vents in Lake Baikal, U.S.S.R. 72:585-589. https://doi.org/10.1029/90EO00409

Dare SAS, Barnes S-J, Beaudoin G (2012) Variation in trace element content of magnetite crystallized from a fractionating sulfide liquid, Sudbury, Canada: implications for provenance discrimination. Geochimica et Cosmochimica Acta 88:27–50. https://doi.org/10.1016/j.gca.2012.04.032

Dare SAS, Barnes S-J, Beaudoin G, Méric J, Boutroy E, Potvin-Doucet C (2014) Trace elements in magnetite as petrogenetic indicators. Miner Depos 49:785–796. https://doi.org/10.1007/s00126-014-0529-0

de Ronde CEJ, Walker SL, Ditchburn RG, Tontini FC, Hannington MD, Merle SG, Timm C, Handler MR, Wysoczanski RJ, Dekov VM, Kamenov GD, Baker ET, Embley RW, Lupton JE, Stoffers P (2014) The anatomy of a buried submarine hydrothermal system, Clark Volcano, Kermadec Arc, New Zealand. Econ Geol 109:2261–2292. https://doi.org/10.2113/econgeo.109.8.2261

Dekov VM, Savelli C (2004) Hydrothermal activity in the SE Tyrrhenian Sea: an overview of 30 years of research. Marine Geol 204:161–185. https://doi.org/10.1016/s0025-3227(03)00355-4

Dekov VM, Kamenov GD, Abrasheva MD, Capaccioni B, Munnik F (2013) Mineralogical and geochemical investigation of seafloor massive sulfides from Panarea Platform (Aeolian Arc, Tyrrhenian Sea). Chem Geol 335:136–148. https://doi.org/10.1016/j.chemgeo.2012.10.048

Ding T, Ma D, Lu J, Zhang R (2018) Magnetite as an indicator of mixed sources for W-Mo–Pb–Zn mineralization in the Huangshaping polymetallic deposit, southern Hunan Province, China. Ore Geol Rev 95:65–78. https://doi.org/10.1016/j.oregeorev.2018.02.019

Domeier M, Torsvik TH (2014) Plate tectonics in the late Paleozoic. Geosci Front 5:303–350. https://doi.org/10.1016/j.gsf.2014.01.002

Dong R, Wang H, Li W, Yan Q-H, Zhang X (2021) The geology, magnetite geochemistry, and oxygen isotopic composition of the Akesayi skarn iron deposit, Western Kunlun Orogenic Belt, Xinjiang, northwest China: implications for ore genesis. Ore Geology Reviews 130:103854. https://doi.org/10.1016/j.oregeorev.2020.103854

Dupuis C, Beaudoin G (2011) Discriminant diagrams for iron oxide trace element fingerprinting of mineral deposit types. Miner Depos 46:319–335. https://doi.org/10.1007/s00126-011-0334-y

Elders WA (1979) The geological background of the geothermal fields of the Salton Trough. In Elders, W A (eds.), Geology and geothermics of the Salton trough. University of California (Riverside), Campus Museum Contribution 5, Geological Society of America Guidebook, Field Trip, 7:108

Fa H and Chaohua, G (1983) Makeng iron deposit-a submarine volcanic hydrothermal- sedimentary ore: Science in China, Ser.B. 1075-1087.

Falkenberg JJ, Keith M, Haase KM, Bach W, Klemd R, Strauss H, Yeo IA, Rubin KH, Storch B, Anderson MO (2021) Effects of fluid boiling on Au and volatile element enrichment in submarine

arc-related hydrothermal systems. Geochimica et Cosmochimica Acta 307:105–132. https://doi.org/10.1016/j.gca.2021.05.047
Fan HR, Hu FF, Yang KF, Pirajno F, Liu X, Wang KY (2014) Integrated U-Pb and Sm–Nd geochronology for a REE-rich carbonatite dyke at the giant Bayan Obo REE deposit, Northern China. Ore Geol Rev 63:510–519. https://doi.org/10.1016/j.oregeorev.2014.03.005
Franklin JM, Gibson HL, Jonasson IR, Galley AG (2005) Volcanogenic massive sulfide deposits. Econ Geol. https://doi.org/10.5382/av100.17
Fricke H, Giere O, Stetter K, Alfredsson GA, Kristjansson JK, Stoffers P, Svavarsson J (1989) Hydrothermal vent communities at the shallow subpolar Mid-Atlantic Ridge. Marine Biol 102:425–429. https://doi.org/10.1007/bf00428495
Fryer BJ, Taylor RP (1984) Sm-Nd direct dating of the Collins Bay hydrothermal uranium deposit, Saskatchewan. Geology 12:479–482. https://doi.org/10.1130/0091-7613
Fu J, Liang X, Wang C, Zhou Y, Jiang Y, Dong C (2017) The Xitieshan volcanic sediment-hosted massive sulfide deposit, North Qaidam, China: Geology, structural deformation and geochronology. Ore Geol Rev 80:923–946. https://doi.org/10.1016/j.oregeorev.2016.08.027
Galley AG, Hannington MD, Jonasson IRH, Jonasson IR (2007) Volcanogenic massive sulphide deposits. doi: https://silversprucerесources.com/site/assets/files/5585/vms-deposits-canada-review.pdf.
Gao B, Chen J, Huang X, Xin H, Zheng Q (2022) Resolving the tectonic setting of South China in the Late Paleozoic. Geophys Res Lett. 49:e2022 GL099809. https://doi.org/10.1029/2022GL099809
Geological Team of the Bereau of geology and mineral resources of Guangdong Province (1988) Detailed geological report of Yushui copper polymetallic mining area in Meixia County. Unpublished, Guangdong Province
German CR, Petersen S, Hannington MD (2016) Hydrothermal exploration of mid-ocean ridges: where might the largest sulfide deposits be forming? Chem Geol 420:114–126. https://doi.org/10.1016/j.chemgeo.2015.11.006
Gibson HL (2007) The VMS model: advances and application to exploration targeting. Ore Deposits and Exploration Technology
Goodfellow WD, McCutcheon SR, Goodfellow WD, McCutcheon SR, Peter JM (2003) Geologic and genetic attributes of volcanic sediment-hosted massive sulfide deposits of the Bathurst Mining Camp, Northern New Brunswick—a synthesis, massive sulfide deposits of the Bathurst Mining Camp, New Brunswick, and Northern Maine. Soc Econ Geol
Grenne T, Slack JF (2005) Geochemistry of jasper beds from the Ordovician Løkken ophiolite, Norway: origin of proximal and distal siliceous exhalites. Econ Geol 100:1511–1527. https://doi.org/10.2113/gsecongeo.100.8.1511
Gu LX, Xu KQ (1986) On the South China type massive sulfide ore deposits formed in marine fault depression troughs on the continental crust. Miner Depos 5(2):1–13 (in Chinese with English abstract)
Gu L, Khin Z, Hu W, Zhang K, Ni P, He J, Xu Y, Lu J, Lin C (2007) Distinctive features of Late Paleozoic massive sulfide deposits in South China. Ore Geol Rev 31:107–138. https://doi.org/10.1016/j.oregeorev.2005.01.002
Guo WM (2010) Metallogenic mechanism, petrogeochemistry and mineralogy of Dongguashan deposit in Tongling, Anhui Province (doctoral dissertation). Supervisor: Lu J J. Nanjing: Nanjing University (in Chinese with English abstract)
Guo W, Lu J, Jiang S, Zhang R, Qi L (2011) Re-Os isotope dating of pyrite from the footwall mineralization zone of the Xinqiao deposit, Tongling, Anhui Province: geochronological evidence for submarine exhalative sedimentation. Chin Sci Bull 56:3860–3865. https://doi.org/10.1007/s11434-011-4770-y
Halley SW, Roberts RH (1997) Henty; a shallow-water gold-rich volcanogenic massive sulfide deposit in western Tasmania. Econ Geol 92:438–447. https://doi.org/10.2113/gsecongeo.92.4.438
Hamilton PJ, O'Nions RK, Evensen NM (1977) Sm-Nd dating of Archaean basic and ultrabasic volcanics. Earth Planet Sci Lett 36:263–268. https://doi.org/10.1016/0012-821X(77)90208-4
Hamilton PJ, Evensen NM, O'Nions RK, Tarney J (1979) Sm—Nd systematics of Lewisian gneisses: implications for the origin of granulites. Nature 277:25–28. https://doi.org/10.1038/277025a0
Hannington MD (2021) VMS and SEDEX Deposits: 867-876
Hannington MD, Poulsen KH, Thompson JFH, Sillitoe RH (1997) Volcanogenic gold in the massive sulfide environment, volcanic associated massive sulfide deposits: processes and examples in modern and ancient settings. Soc Econ Geol, pp 0
Hannington MD, Bleeker W, Kjarsgaard I, Hannington MD, Barrie, CT (1999a) Sulfide mineralogy, geochemistry, and ore genesis of the Kidd Creek deposit: part I. North, Central, and South Orebodies, The Giant Kidd Creek Volcanogenic Massive Sulfide Deposit, Western Abitibi Subprovince, Canada. Society of Economic Geologists, pp 0
Hannington MD, Bleeker W, Kjarsgaard I, Barrie CT (1999b) Sulfide mineralogy, geochemistry, and ore genesis of the Kidd Creek deposit: part II The Bornite Zone, The Giant Kidd Creek Volcanogenic Massive Sulfide Deposit, Western Abitibi Subprovince, Canada. Society of Economic Geologists, pp 0
Hannington MD, Barrie CT, Bleeker W (1999c) The giant Kidd Creek volcanogenic massive sulfide deposit, western Abitibi Subprovince, Canada: summary and synthesis, The Giant Kidd Creek Volcanogenic Massive Sulfide Deposit, Western Abitibi Subprovince, Canada. Society of Economic Geologists, pp 0
Hannington MD, De Ronde CEJ, Petersen S (2005) Sea-floor tectonics and submarine hydrothermal systems. Econ Geol. https://doi.org/10.5382/av100.06
Hannington MD, Jamieson J, Monecke T, Petersen S, Beaulieu S (2011) The abundance of seafloor massive sulfide deposits. Geology 39:1155–1158. https://doi.org/10.1130/g32468.1
Hao TP (1993) Sm-Nd isotopic ages of Proterozoic metamorphic rocks from the middle sector of the Jinsha River. Geol Rev. 39:52–56 (in Chinese with English abstract)
He YJ (1990) Metallogenic-geologic characteristics of Yushui Hydrothermal-sedimentary polymetallic deposit in Meixian county Guangdong Province. Guangdong Geology 3(1):1–13 (in Chinese with English abstract)
Hecht L, Freiberger R, Gilg HA, Grundmann G, Kostitsyn YA (1999) Rare earth element and isotope (C, O, Sr) characteristics of hydrothermal carbonates: genetic implications for dolomite-hosted talc mineralization at Göpfersgrün (Fichtelgebirge, Germany). Chem Geol 155:115–130. https://doi.org/10.1016/S0009-2541(98)00144-2
Heinicke J, Italiano F, Maugeri R, Merkel B, Pohl T, Schipek M, Braun T (2009) Evidence of tectonic control on active arc volcanism: the Panarea-Stromboli tectonic link inferred by submarine hydrothermal vents monitoring (Aeolian arc, Italy). Geophys Res Lett 36. https://doi.org/10.1029/2008gl036664
Herzig PM, Hannington MD (1995) Polymetallic massive sulfides at the modern seafloor a review. Ore Geol Rev 10:95–115. https://doi.org/10.1016/0169-1368(95)00009-7
Hou ZQ, Han F, Xia LQ, Zhang QL, Qu XM, Li ZQ, Bie FL, Wang LQ,Yu JJ, Tang SH (2003) Hydrothermal systems and metallogeny on the modern and ancient sea-floor. Geological Publishing House, Beijing, pp 1–386 (in Chinese)
Hu X, Huang Z, Wang J, Yu J, Xu K, Jansa L, Hu W (2012) Geology of the Fuding inlier in southeastern China: implication for late

Paleozoic Cathaysian paleogeography. Gondwana Res 22:507–518. https://doi.org/10.1016/j.gr.2011.09.016

Hu L, Cawood PA, Du Y, Yang J, Jiao L (2015) Late Paleozoic to Early Mesozoic provenance record of Paleo-Pacific subduction beneath South China. Tectonics 34:986–1008. https://doi.org/10.1002/2014TC003803

Hu X, Chen H, Zhao L, Han J, Xia X (2017) Magnetite geochemistry of the Longqiao and Tieshan Fe–(Cu) deposits in the Middle-Lower Yangtze River Belt: implications for deposit type and ore genesis. Ore Geol Rev 89:822–835. https://doi.org/10.1016/j.oregeorev.2017.07.019

Huang Y (2015) Metallogenic Mechanism of the massive sulfide deposits formed in the fault depression zones on the continental crust-a case study of the Yushui Copper-Polymetallic deposit, Eastern Guangdong Province, China. Doctoral dissertation of Sun Yat-sen University. 1-192 (in Chinese)

Huang XW, Zhou MF, Qiu YZ, Qi L (2015a) In-situ LA-ICP-MS trace elemental analyses of magnetite: the Bayan Obo Fe-REE-Nb deposit, North China. Ore Geol Rev 65:884–899. https://doi.org/10.1016/j.oregeorev.2014.09.010

Huang Y, Sun X, Shi G, Sa R, Guan Y, Jiang X, Que H (2015b) Re–Os dating of sulphides from the Yushui Cu-polymetallic deposit in eastern Guangdong Province, South China. Ore Geol Rev 70:281–289. https://doi.org/10.1016/j.oregeorev.2015.04.018

Huang XW, Boutroy É, Makvandi S, Beaudoin G, Corriveau L, De Toni AF (2019a) Trace element composition of iron oxides from IOCG and IOA deposits: relationship to hydrothermal alteration and deposit subtypes. Miner Depos 54:525–552. https://doi.org/10.1007/s00126-018-0825-1

Huang Y, Wu Z, Sun X, Wang Y, Shi G, Zhai W, Guan Y (2019b) He-Ar isotopes and trace gas compositions of fluid inclusions in massive sulphides from the Yushui copper-polymetallic deposit. South China: Metallogenic implications. Minerals 9. https://doi.org/10.3390/min9050258

Isley AE (1995) Hydrothermal plumes and the delivery of iron to banded iron formation. J Geol 103:169–185. https://doi.org/10.1086/629734

Isozaki Y, Aoki K, Nakama T, Yanai S (2010) New insight into a subduction-related orogen: a reappraisal of the geotectonic framework and evolution of the Japanese Islands. Gondwana Res 18:82–105. https://doi.org/10.1016/j.gr.2010.02.015

Jedwab J, Blanc G, Boulegue J (1989) Vanadiferous minerals from the Nereus Deep, Red Sea. Terra Nova 1:188–194. https://doi.org/10.1111/j.1365-3121.1989.tb00351.x

Jia L, Mao J, Liu P, Li Y (2018) Petrogenesis of the late Early Cretaceous granodiorite – quartz diorite from eastern Guangdong, SE China: implications for tectono–magmatic evolution and porphyry Cu–Au–Mo mineralization. Lithos 304–307:388–411. https://doi.org/10.1016/j.lithos.2018.02.008

Jiang SY, Han F, Shen JZ, Palmer MR (1999) Chemical and Rb–Sr, Sm–Nd isotopic systematics of tourmaline from the Dachang Sn-polymetallic ore deposit, Guangxi Province, P.R China. Chem Geol 157:49–67. https://doi.org/10.1016/S0009-2541(98)00200-9

Jiang SY, Slack JF, Palmer MR (2000) Sm-Nd dating of the giant Sullivan Pb-Zn-Ag deposit British Columbia. Geology 28:8. https://doi.org/10.1130/0091-7613

Jiang SY, Sun Y, Sun MZ, Bian LZ, Xiong YG, Yang SY, Luo L, Cao ZQ, Wu YM (2010) Reiterative fault systems and superimposed mineralization in the Jiurui metallogenic cluster district, middle and lower Yangtze river mineralization belt China. Acta Petrologica Sinica 26(9):2751–2767 (in Chinese with English abstract)

Jiang SY, Bian LZ, Ding QF, Yang SY, Zhu ZY, Sun MZ, Sun Y, Xiong YG (2011) Discovery and significance of carbonate mud mounds from Cu-polymetallic deposits in the Middle and Lower Yangtze River mineralization belt: examples from the Wushan and Dongguashan deposits. Acta Geologica Sinica 85(5):744–756 (in Chinese with English abstract)

Kempe U, Belyatsky B, Krymsky R, Kremenetsky A, Ivanov P (2001) Sm–Nd and Sr isotope systematics of scheelite from the giant Au(–W) deposit Muruntau (Uzbekistan): implications for the age and sources of Au mineralization. Miner Depos 36:379–392. https://doi.org/10.1007/s001260100156

Kimberley MM (1989) Exhalative origins of iron formations. Ore Geol Rev 5:13–145. https://doi.org/10.1016/0169-1368(89)90003-6

Kong FB, Jiang SY, Xu YM, Zhu ZY, Qian HD, Bian LZ (2012) Submarine hydrothermal exhalation with superimposed magmatic-hydrothermal mineralization in the Wushan copper deposit, Jiangxi province: constraints from geological, ore texture and ore deposit geochemistry. Acta Petrologica Sinica 28(12):3929–3937 (in Chinese with English abstract)

Li DF, Chen HY, Hollings P, Zhang L, Sun XM, Zheng Y, Xia XP, Xiao B, Wang CM, Fang J (2018) Trace element geochemistry of magnetite: implications for ore genesis of the Talate skarn Pb-Zn (-Fe) deposit, Altay, NW China. Ore Geol Rev 100:471–482. https://doi.org/10.1016/j.oregeorev.2017.03.015

Li SS, Chen HY, Peng YX, Wang LM, Luo ZR (2019) Tectonic evolution of the Yongmei depression constrained by zircon LA-ICP-MS U-Pb ages of granite porphyry and diabase from the Yushui Cu-Pb-Zn polymetallic deposit. Geochimica 48(4):313–324 (in Chinese with English abstract)

Liu JQ (1997) Thermobarogeochemistry, ore-forming age and genesis study for the Yushui copper-rich multimetal deposit in Meixian county, Guangdong Province, Southern China. Geol Min Resour South China 1:37–50 (in Chinese with English abstract)

Liu Y, Hu Z, Gao S, Günther D, Xu J, Gao C, Chen H (2008) In situ analysis of major and trace elements of anhydrous minerals by LA-ICP-MS without applying an internal standard. Chem Geol 257:34–43. https://doi.org/10.1016/j.chemgeo.2008.08.004

Liu Y, Hu Z, Zong K, Gao C, Gao S, Xu J, Chen H (2010) Reappraisement and refinement of zircon U-Pb isotope and trace element analyses by LA-ICP-MS. Chin Sci Bull 55:1535–1546. https://doi.org/10.1007/s11434-010-3052-4

Liu P, Mao J, Santosh M, Bao Z, Zeng X, Jia L (2018) Geochronology and petrogenesis of the Early Cretaceous A-type granite from the Feie'shan W-Sn deposit in the eastern Guangdong Province, SE China: implications for W-Sn mineralization and geodynamic setting. Lithos 300–301:330–347. https://doi.org/10.1016/j.lithos.2017.12.015

Liu WG, Li ZD, Wei S, Chen J, Liu Y, Ao C, Xiao ZB, Zhou HY, Liu H (2019) Rapid separation and precise determination of strontium isotopic from geological samples with high rubidium/strontium ratios. Chin J Analytic Chem 47:1054–1060. https://doi.org/10.1016/s1872-2040(19)61172-2

Liu P, Gu X, Zhang W, Hu H, Chen X, Wang X, Song W, Yu M, Cook NJ (2023) Jingwenite-(Y) from the Yushui Cu deposit, South China: the first occurrence of a V-HREE-bearing silicate mineral. Am Min 108:192–196. https://doi.org/10.2138/am-2022-8373

Liu P, Gleeson SA, Cook NJ, Lehmann B, Zhao C, Yao W, Bao ZA, Wu ST, Tian YF, Mao JW (2023) Final assembly of Gondwana enhances crustal metal (HREE and U) endowment. Geochem Perspect Lett 26:7–13. https://doi.org/10.7185/geochemlet.2317

Ludwig KR (2003) User's Manual for Isoplot 3.00, a geochronological Toolkit for Microsoft Excel. Berkeley Geochronological Center Special Publication 4:25–32

Lusty PAJ, Lacinska AM, Millar IL, Barrie CD, Boyce AJ (2017) Volcanological and environmental controls on the Snowdon mineralization, North Wales, UK: a failed volcanogenic massive sulfide system in the Avalon Zone of the British Caledonides. Ore Geol Rev 89:557–586. https://doi.org/10.1016/j.oregeorev.2017.06.031

Maas R, Apukhtina OB, Kamenetsky VS, Ehrig K, Sprung P, Münker C (2022) Carbonates at the supergiant Olympic Dam Cu-U-Au-Ag deposit, South Australia part 2: Sm-Nd, Lu-Hf and Sr-Pb isotope constraints on the chronology of carbonate deposition. Ore Geol Rev 140:103745. https://doi.org/10.1016/j.oregeorev.2020.103745

Makvandi S, Ghasemzadeh-Barvarz M, Beaudoin G, Grunsky EC, McClenaghan MB, Duchesne C, Boutroy E (2016) Partial least squares-discriminant analysis of trace element compositions of magnetite from various VMS deposit subtypes: application to mineral exploration. Ore Geol Rev 78:388–408. https://doi.org/10.1016/j.oregeorev.2016.04.014

Marani MP, Gamberi F, Savelli C (1997) Shallow-water polymetallic sulfide deposits in the Aeolian island arc. Geology 25:9. https://doi.org/10.1130/0091-7613

Marani M, Gamberi F, Bonatti E, De Alteris G, Magagnoli A, Monteduro R, Tonielli R, Scotto di Vetimo P (2002) ROV observations of the anomalous submarine gas venting occurring in the Lisca Bianca, Bottaro and Lisca Nera areas of the Panarea Island platform. http://www.bo.ismar.cnr.it/FS_ricerca.htm

Matthews A (1976) Magnetite formation by the reduction of hematite with iron under hydrothermal conditions. American Mineralogist 61:927-932. http://www.minsocam.org/MSA/AmMin/TOC/

McKibben MA, Elders WA (1985) Fe-Zn-Cu-Pb mineralization in the Salton Sea geothermal system, Imperial Valley, California. Econ Geol 80:539–559. https://doi.org/10.2113/gsecongeo.80.3.539

Meinert LD, Dipple GM, Nicolescu S, Hedenquist JW, Thompson JFH, Goldfarb RJ, Richards JP (2005) World skarn deposits. Society of Economic Geologists, One Hundredth Anniversary Volume

Metcalfe I (2013) Gondwana dispersion and Asian accretion: tectonic and paleogeographic evolution of eastern Tethys. J Asian Earth Sci 66:1–33. https://doi.org/10.1016/j.jseaes.2012.12.020

Monecke T, Petersen S, Hannington MD (2014) Constraints on water depth of massive sulfide formation: evidence from modern seafloor hydrothermal systems in arc-related settings. Econ Geol 109:2079–2101. https://doi.org/10.2113/econgeo.109.8.2079

Nie FJ, BjφRlykke A, Nilsen KS (1999) The origin of the Proterozoic Bidjovagge gold-copper deposit, Finnmark, Northern Norway, as deduced from rare earth element and Nd isotopic evidences on calcites. Resour Geol 49:13–25. https://doi.org/10.1111/j.1751-3928.1999.tb00028.x

No. 723 Team of Guangdong Bureau of Geology and Mineral Resource (BGMR)(1988) Geological report of Yushui copper polymetallic mining area in Meixian County, internal data: Guangdong Province, 1-298 (in Chinese)

Ohmoto H (1996) Formation of volcanogenic massive sulfide deposits: the Kuroko perspective. Ore Geol Rev 10:135–177. https://doi.org/10.1016/0169-1368(95)00021-6

Ohmoto H (2003) Nonredox transformations of magnetite-hematite in hydrothermal systems. Econ Geol 98:157–161. https://doi.org/10.2113/gsecongeo.98.1.157

Olafsson J, Honjo S, Thors K, Stefansson U, Jones R, Ballard RD (1989) Initial observation, bathymetry and photography of a geothermal site on the Kolbeinsey Ridge. Oceanography 1988:121–127

Otake T, Wesolowski DJ, Anovitz LM, Allard LF, Ohmoto H (2010) Mechanisms of iron oxide transformations in hydrothermal systems. Geochimica et Cosmochimica Acta 74:6141–6156. https://doi.org/10.1016/j.gca.2010.07.024

Palmer MR, Edmond JM (1989) The strontium isotope budget of the modern ocean. Earth Planet Sci Lett 92:11–26. https://doi.org/10.1016/0012-821X(89)90017-4

Peng JT, Hu RZ, Burnard PG (2003) Samarium–neodymium isotope systematics of hydrothermal calcites from the Xikuangshan antimony deposit (Hunan, China): the potential of calcite as a geochronometer. Chem Geol 200:129–136. https://doi.org/10.1016/S0009-2541(03)00187-6

Peng HJ, Hou L, Sun C, Zou H, Wang TR, Ma Z-Z (2021) Geochemistry of magnetite from the Hongniu-Hongshan Cu skarn deposit in Yunnan Province SW China. Ore Geol Rev 136:104237. https://doi.org/10.1016/j.oregeorev.2021.104237

Peter JMJG (2003) Ancient iron formations: their genesis and use in the exploration for stratiform base metal sulfide deposits, with examples from the Bathurst Mining Camp. 4,145-176

Petersen S, Krätschell A, Augustin N, Jamieson J, Hein JR, Hannington MD (2016) News from the seabed – geological characteristics and resource potential of deep-sea mineral resources. Marine Policy 70:175–187. https://doi.org/10.1016/j.marpol.2016.03.012

Pirajno F, Cawood PA (2009) Hydrothermal processes and mineral systems. Springer

Pirajno F, Chen Y, Li N, Li C, Zhou L (2016) Besshi-type mineral systems in the Palaeoproterozoic Bryah rift-basin, Capricorn Orogen, Western Australia: Implications for tectonic setting and geodynamic evolution. Geosci Front 7:345–357. https://doi.org/10.1016/j.gsf.2015.09.003

Ren JS (1990) On the geotectonics of southern China. Acta Geologica Sinica 4:275–288 (in Chinese with English abstract)

Ridler R (1971) Analysis of Archean volcanic basins in Canadian Shield using exhalite concept, Canadian Mining And Metallurgical Bulletin, Canadian Inst Mining Metallurgy Petroleum 101 6th Ave Sw, Ste 320, Calgary, pp 20

Sánchez V, Cardellach E, Corbella M, Vindel E, Martín-Crespo T, Boyce AJ (2010) Variability in fluid sources in the fluorite deposits from Asturias (N Spain): further evidences from REE, radiogenic (Sr, Sm, Nd) and stable (S, C, O) isotope data. Ore Geol Rev 37:87–100. https://doi.org/10.1016/j.oregeorev.2009.12.001

Sangster DF (1980) Quantitative characteristics of volcanogenic massive sulfide deposits: Bulletin of Canada Institute Mineral Metallurgy 73:74–81

Sappin AA, Dupuis C, Beaudoin G, Pozza M, McMartin I, McClenaghan MB (2014) Optimal ferromagnetic fraction in till samples along ice-flow paths: case studies from the Sue-Dianne and Thompson deposits, Canada. Geochemistry: Exploration. Environment, Analysis 14:315–329. https://doi.org/10.1144/geochem2013-212

Savelli C, Marani M, Gamberi F (1999) Geochemistry of metalliferous, hydrothermal deposits in the Aeolian arc (Tyrrhenian Sea). J Volcanol Geotherm Res 88:305–323. https://doi.org/10.1016/S0377-0273(99)00007-4

Schaarschmidt A, Haase KM, Klemd R, Keith M, Voudouris PC, Alfieris D, Strauss H, Wiedenbeck M (2021) Boiling effects on trace element and sulfur isotope compositions of sulfides in shallow-marine hydrothermal systems: evidence from Milos Island Greece. Chem Geol 583:120457. https://doi.org/10.1016/j.chemgeo.2021.120457

Schulz K (2010) Regional environment in volcanogenic massive sulfide occurrence model. Geological Survey Scientific Investigations Report 2010–5070 –C, chap. 4. p 24

Shanks W (2012) Hydrothermal alteration in volcanogenic massive sulfide occurrence model. US Geol Surv Sci Investig Rep 2010-5070-C:165–180

Shanks IW, Callender E (1992) Thermal springs in Lake Baikal. Geology 20:495. https://doi.org/10.1130/0091-7613

Shen L, Yu JH, O'Reilly SY, Griffin WL (2018) Tectonic switching of Southeast China in the Late Paleozoic. J Geophys Res Solid Earth 123:8508–8526. https://doi.org/10.1029/2018jb015520

Slack JFJD, Rocks GMfC-C-GDiM (2012) 3. Historical evolution of descriptive and genetic knowledge and concepts in volcanogenic massive sulfide occurrence model: U.S. Geological Survey Scientific Investigations Report 2010–5070 –C, chap. 3, pp 6

Spry PG, Peter JM (2000) Meta-exhalites as exploration guides to ore. 11:163–201

Su W, Hu R, Xia B, Xia Y, Liu Y (2009) Calcite Sm-Nd isochron age of the Shuiyindong Carlin-type gold deposit, Guizhou, China. Chem Geol 258:269–274. https://doi.org/10.1016/j.chemgeo.2008.10.030

Tanaka T, Togashi S, Kamioka H, Amakawa H, Kagami H, Hamamoto T, Yuhara M, Orihashi Y, Yoneda S, Shimizu H, Kunimaru T, Takahashi K, Yanagi T, Nakano T, Fujimaki H, Shinjo R, Asahara Y, Tanimizu M, Dragusanu C (2000) JNdi-1: a neodymium isotopic reference in consistency with LaJolla neodymium. Chem Geol 168:279–281. https://doi.org/10.1016/S0009-2541(00)00198-4

Tiercelin JJ, Pflumio C, Castrec M, Boulégue J, Gente P, Rolet J, Coussement C, Stetter KO, Huber R, Buku S, Mifundu W (1993) Hydrothermal vents in Lake Tanganyika, East African Rift system. Geology 21:499. https://doi.org/10.1130/0091-7613(1993)021%3c0499:hvilte%3e2.3.co;2

Tornos F (2006) Environment of formation and styles of volcanogenic massive sulfides: the Iberian Pyrite Belt. Ore Geol Rev 28:259–307. https://doi.org/10.1016/j.oregeorev.2004.12.005

Tornos F, Spiro B (1997) The carbonate-rich hydrothermal alteration related to the massive sulfides in the Iberian Pyrite Belt. Abstract Volume, Society of Economic Geologists Field Conference, 82

Tornos F, Spiro B, Stanley Cjmdptpr, Balkema (1999) The genesis of shale-hosted massive sulfides in the Iberian Pyrite Belt. 605-608

Veizer J (1989) Strontium isotopes in seawater through time. Annual Rev Earth Planet Sci 17:141–167. https://doi.org/10.1146/annurev.ea.17.050189.001041

Veizer J, Ala D, Azmy K, Bruckschen P, Buhl D, Bruhn F, Carden G, Diener A, Ebneth S, Godderis Y, Jasper T, Korte C, Pawellek F, Podlaha OG, Strauss H (1999) $^{87}Sr/^{86}Sr$, $\delta^{13}C$ and $\delta^{18}O$ evolution of Phanerozoic seawater. Chem Geol 161:59–88. https://doi.org/10.1016/S0009-2541(99)00081-9

Verdugo-Ihl MR, Ciobanu CL, Courtney-Davies L, Cook NJ, Slattery A, Ehrig K, Tornos F, Hanchar JM (2022) U-Pb geochronology and mineralogy of hematite from Mantoverde and Carmen de Cobre, Northern Chile: constraints on Andean IOCG mineralization. Econ Geol 117:943–960. https://doi.org/10.5382/econgeo.4903

Wang SX (2005) On spatial distribution and signification of Carboniferous marine volcanic rocks in the Southwest Fujian depression. Geol Fujian 22(04):217–220 (in Chinese with English abstract)

Wang Y, Jin Y (2000) Permian paleogeographic evolution of the Jiangnan Basin, South China. Palaeogeogr Palaeoclimatol Palaeoecol 160:35–44. https://doi.org/10.1016/S0031-0182(00)00043-2

Wang LM, Yang M, Peng SL (1999) On the genesis of the Yushui polymetallic deposit in Meixian county Guangdong Province. Geotectonica et Metallogenia 23(4):345–352 (in Chinese with English abstract)

Wang S, Zhang D, Wu G, Vatuva A, Di Y, Yan P, Feng H, Ma S (2017) Late Paleozoic to Mesozoic extension in southwestern Fujian Province, South China: geochemical, geochronological and Hf isotopic constraints from basic-intermediate dykes. Geosci Front 8:529–540. https://doi.org/10.1016/j.gsf.2016.05.005

Wang YJ, Zhu WG, Huang HQ, Bai ZJ, Zhong H, Yao JH, Fan HP (2020) Geochemistry of magnetite from the giant Paleoproterozoic Dahongshan Fe-Cu deposit, SW China: constraints on nature of ore-forming fluids and depositional setting. Ore Geol Rev 118:103361. https://doi.org/10.1016/j.oregeorev.2020.103361

Wen G, Li JW, Hofstra AH, Koenig AE, Lowers HA, Adams D (2017) Hydrothermal reequilibration of igneous magnetite in altered granitic plutons and its implications for magnetite classification schemes: insights from the Handan-Xingtai iron district, North China Craton. Geochimica et Cosmochimica Acta 213:255–270. https://doi.org/10.1016/j.gca.2017.06.043

Wilson Marjorie (1989) Mid-ocean ridges In: Wilson M (ed) Igneous Petrogenesis. Springer Netherlands, Dordrecht, pp 101-150. https://doi.org/10.1007/978-1-4020-6788-4_5

Wilson IF, Rocha VS (1955) Geology and mineral deposits of the Boleo copper district, Baja California, Mexico. US Government Printing Office

Xie HG, Wang WB, Li WD (1995) The genesis and metallogenetic epoch of Xinqiao Cu-S deposit Anhui. Volcanol Miner Resour 16(2):101–107 (in Chinese with English abstract)

Xing B, Mao J, Xiao X, Liu H, Yu L, Li H, Guo S, Li H, Huang W (2022) Genesis of the Dingjiashan and Fengyan Zn-Pb polymetallic deposits in central Fujian, SE China: evidence from magnetite geochemistry. Ore Geol Rev 144:104851. https://doi.org/10.1016/j.oregeorev.2022.104851

Xun Z, Allen MB, Whitham AG, Price SP (1996) Rift-related Devonian sedimentation and basin development in South China. J Southeast Asian Earth Sci 14:37–52. https://doi.org/10.1016/s0743-9547(96)00020-7

Yi JJ (2018) Study on the genetic mechanism and prospecting model of Makeng iron deposit in Southwest Fujian. China University of Geosciences (Beijing)

Zhang CS (2012) Geology and geochemistry of Makeng Fe-Mo deposit, Fujian. Doctoral dissertation of China University of Geosciences. 1-199(in Chinese with English abstract)

Zhao WW, Zhou MF (2015) In-situ LA–ICP-MS trace elemental analyses of magnetite: the Mesozoic Tengtie skarn Fe deposit in the Nanling Range, South China. Ore Geol Rev 65:872–883. https://doi.org/10.1016/j.oregeorev.2014.09.019

Zhao X, Allen MB, Whitham AG, Price SP (1996) Rift-related Devonian sedimentation and basin development in South China. J Southeast Asian Earth Sci 14:37–52. https://doi.org/10.1016/s0743-9547(96)00020-7

Zhao JH, Zhou MF, Zheng JP (2010) Metasomatic mantle source and crustal contamination for the formation of the Neoproterozoic mafic dike swarm in the northern Yangtze Block, South China. Lithos 115:177–189. https://doi.org/10.1016/j.lithos.2009.12.001

Zhou H, Sun X, Wu Z, Liao J, Fu Y, Li D, Hollings P, Liu Y, Lin H, Lin Z (2017) Hematite U-Pb geochronometer: insights from monazite and hematite integrated chronology of the Yaoan gold deposit, Southwest China. Econ Geol 112:2023–2039. https://doi.org/10.5382/econgeo.2017.4539

Zindler A, Hart S (1986) Chemical geodynamics. Annual Rev Earth Planet Sci 14:493–571. https://doi.org/10.1146/annurev.ea.14.050186.002425

Publisher's Note Springer Nature remains neutral with regard to jurisdictional claims in published maps and institutional affiliations.

Springer Nature or its licensor (e.g. a society or other partner) holds exclusive rights to this article under a publishing agreement with the author(s) or other rightsholder(s); author self-archiving of the accepted manuscript version of this article is solely governed by the terms of such publishing agreement and applicable law.